5-21-2014 12:00 AM

MR to Ultrasound Registration for Image-Guided Prostate Biopsy

Yue Sun
The University of Western Ontario

Supervisor
Dr. Aaron Fenster
The University of Western Ontario

Graduate Program in Biomedical Engineering
A thesis submitted in partial fulfillment of the requirements for the degree in Master of Engineering Science
© Yue Sun 2014

MR TO ULTRASOUND REGISTRATION FOR IMAGE-GUIDED PROSTATE BIOPSY

(Thesis format: Integrated Article)

by

Yue <u>Sun</u>

Biomedical Engineering Graduate Program

A thesis submitted in partial fulfillment

of the requirements for the degree of

Masters of Engineering Science

The School of Graduate and Postdoctoral Studies

The University of Western Ontario

London, Ontario, Canada

© Yue Sun 2014

Abstract

Two dimensional (2D) transrectal ultrasound (TRUS) guided prostate biopsy is the standard approach for definitive diagnosis of prostate cancer (PCa). However, due to the lack of image contrast of prostate tumors needed to clearly visualize early-stage PCa, prostate biopsy often results in false negatives, requiring repeat biopsies. Magnetic Resonance Imaging (MRI) has been considered to be a promising imaging modality for noninvasive identification of PCa, since it can provide a high sensitivity and specificity for the detection of early stage PCa. Our main objective is to develop and validate a registration method of 3D MR-TRUS images, allowing generation of volumetric 3D maps of targets identified in 3D MR images to be biopsied using 3D TRUS images. We proposed an image-based non-rigid registration approach which employs the multi-channel modality independent neighborhood descriptor (MIND) as the local similarity feature across the two modalities of MR and TRUS. A novel and efficient duality-based convex optimization-based algorithmic scheme was introduced to extract the deformations and align the two MIND descriptors. The registration accuracy was evaluated using 20 patient images by calculating the target registration error (TRE) using manually identified corresponding intrinsic fiducials in the whole gland and peripheral zone. Additional performance metrics (DSC, MAD, and MAXD) were also calculated by comparing the MR and TRUS manually segmented prostate surfaces in the registered images. Experimental results showed that the proposed method yielded an overall median TRE of 1.76 mm. In addition, we proposed a surface-based registration method, which first makes use of an initial rigid registration of 3D MR images to 3D TRUS images using 6 manually

placed approximately corresponding landmarks in each image. Following the manual initialization, two prostate surfaces are segmented from 3D MR and TRUS images and then non-rigidly registered using a thin-plate spline (TPS) algorithm. The registration accuracy was evaluated using 17 patient images by measuring TRE. Experimental results show that the proposed method yielded an overall mean TRE of 2.24 mm, which is favorably comparable to a clinical requirement for an error of less than 2.5 mm.

Co-Authorship Statement

This thesis is an integration of two articles, each constituting a chapter; the journal publications listed in the following are either in revision, or in preparation for submission.

Chapter 2: Three-Dimensional Non-Rigid MR-TRUS Registration Using Dual Optimization, submitted to the IEEE Transactions on Medical Imaging, November, 2013 - is currently under revision (Manuscript#2013-0816).

Preliminary version of this work was published in the proceedings of Medical Image Computing and Computer Assistant Intervention (MICCAI), 2013. My contributions for this work included data preparation, development of software to perform image registration, manual identification of fiducials for validation, implementation of software for results analysis and validation, and manuscript preparation. J.Yuan developed and implemented the optimization algorithm. C. Romagnoli was involved in clinical image acquisitions. All authors helped in the manuscript preparation and review. The work was performed under the supervision of A. Fenster.

Chapter 3: 3D Surface-Based Non-Rigid MR-TRUS Registration for Image-Guided Prostate Biopsy, is currently under preparation to Medical Physics.

My contributions for this work included data preparation, development and implementation of registration algorithms, writing software code to perform validation, and manuscript preparation. W. Qiu provided segmentation perspectives with many brainstorming sessions. C. Romagnoli was involved in clinical image acquisitions. All authors helped in the manuscript preparation and review. The work was performed under the supervision of A. Fenster.

iv

Acknowledgements

First and foremost, I would like to thank my supervisor Dr. Aaron Fenster for giving me the chance to study in a world-leading lab, as well as his support, guidance and confidence in me. What I learned from him was not only academic knowledge, but the positive attitude and the passion towards science. No matter how busy his schedule was, he always made time to answer my questions, helped me explore ideas, edited my papers on the weekends and afforded me endless patience and encouragement. To me, it is a treasure for a lifetime to be one of his students, and to be a part of Fenster group. I would like to sincerely thank Dr. Jing Yuan for his guidance and support. For the hours Dr. Yuan spent in helping me prepare papers, explaining mathmetics, and answering so many of my questions, I am greatly indebted.

I would like to acknowledge my advisory committee members, Dr. Cesare Romagnoli for his untiring support of helping me interpret MR and ultrasound images of prostates and finding fiducials, and Dr. Aaron Ward for his insight and feedback. I would like to thank Lori Gardi and Igor Gyacskov for developing the software for prostate segmentation and initialization of prostate registration, and Dr. Wu Qiu and Dr. David Tessier for being the operators for testing the variability of registration initialization and providing general support.

Additionally, I would like to thank all my labmates at Robarts for making my master's life a wonderful experience.

Finally, I would like thank my parents and friends for inspiring me to follow my dreams and being by my side throughout my journey.

Contents

List of Figures

List of Tables

List of Appendices

List of Abbreviations

BPH   benign prostatic hyperplasia

CG   central gland

DCE   dynamic contrast enhanced

DRE   digital rectal exam

DSC   dice similarity coefficient

DWI   diffusion-weighted imaging

FLE   fiducial localization error

ITP   iterative closest point

MR   magnetic resonance

MRI   magnetic resonance imaging

MAD   mean absolute surface distance

MAXD   maximum absolute surface distance

MI   mutual information

MIND   modality independent neighbourhood descriptor

NMI   normalized mutual information

PDE   partial differential equation

PSA   prostate specific antigen

PZ   peripheral zone

RMS   root mean square

TPS   thin plate spline

TRE   target registration error

TRUS   transrectal ultrasound

US   ultrasound

WG   whole gland

Chapter 1

Introduction

1.1 Motivation and Clinical Background Overview

Prostate cancer is the most common non-skin cancer in men in developed countries, with a large and increasing incidence in most countries, and the third leading cause of death due to cancer. It is estimated to affect 26,500 men in Canada in 2012 [1], 238,590 in United States in 2013 [3] and is the most common cancer in men in UK (40,975 new cases in 2010) [2]. Two dimensional (2D) transrectal ultrasound (TRUS) guided prostate biopsy is the standard approach for definitive diagnosis and guiding biopsy needles to suspicious regions in the prostate, due to its real-time, radiation-free, easy-to-perform and -access imaging capability, and low cost. [6]. However, the false-negative rates for systematic sextant biopsies range up to 30% [7] due to a lack of image contrast of prostate tumours that is needed to clearly visualize early-stage prostate cancer. This results in an increasing number of repeat biopsies.

Magnetic Resonance Imaging (MRI) is considered to be a promising imaging modal-

1

ity for noninvasive identification of prostate cancers because of its high sensitivity and specificity for detecting early stage prostate cancer [8]. Reports have shown that multiparametric MR imaging combined with an endorectal coil can achieve a high degree of accuracy (between 79% - 96%) in diagnosing prostate cancer [9] [10] [11].

In terms of diagnostic accuracy and patient comfort, the endorectal coil does not significantly improve the staging of prostate cancer and presents several complications compared to using a pelvic phased-array coil alone [12]. Therefore, a phased-array coil MRI may be a better alternative when considering patient comfort. Although MR prostate imaging is advancing, it cannot replace TRUS guided needle biopsy at this time. This is especially true when real-time guidance is required, and the high cost and time-consuming procedure of performing MR imaging and targeting is taken into consideration.

Thus, the development of an MR-TRUS registration technique is motivated to direct biopsy needles using TRUS toward regions of the prostate containing MR identified suspicious lesions [11], which provides an effective way to perform TRUS-guided biopsy.

Accurate targeting the suspicious lesion identified in the MR image depends on accurate registration of the 3D TRUS and MR images. However, the prostate of the same patient may undergo deformations between the TRUS and MR imaging procedures. This can be due to different patient positioning during the TRUS and MRI procedures, bladder filling, rectal wall motion, and/or the transducer probe pressure shifting and deforming the prostate. In order to compensate for these deformations, non-rigid registration methods are needed for prostate multimodal registration.

Efficient and accurate non-rigid 3D MR-3D TRUS registration is a challenging task due to the totally different appearance of images acquired from these two imaging modal-

ities.

1.2 The Prostate Gland

1.2.1 Anatomy
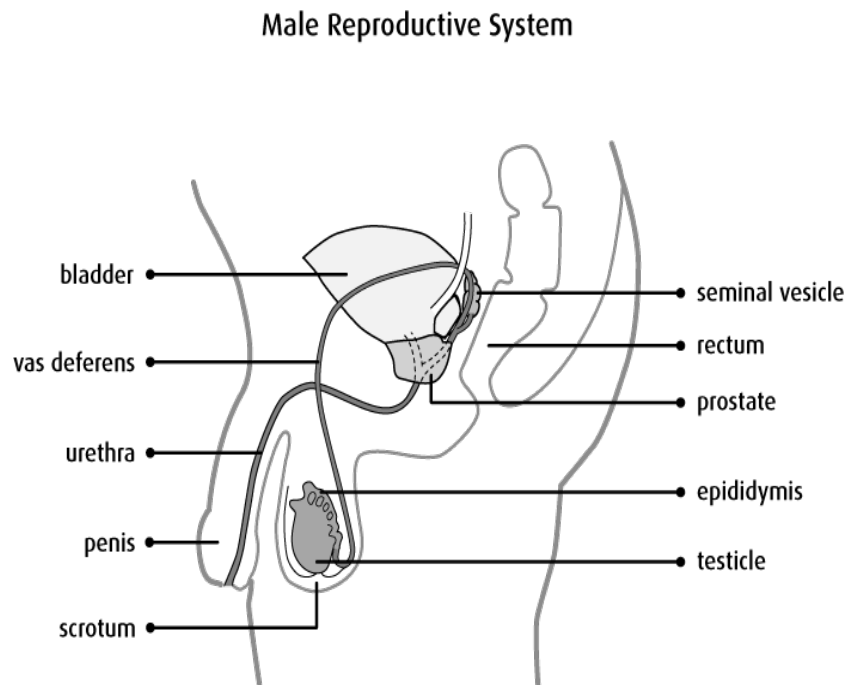
Figure 1.1: Anatomy of the male reproductive and urinary systems, showing the prostate, testicles, bladder, and other organs. [1]

The prostate gland is part of a man's reproductive and urinary systems, which is located between the bladder and the penis, and just in front of the rectum. The actual size of the prostate varies from man to man. It can range from the size of a walnut to a small apple. The normal prostate size for an adult male is 15 cc to 30 cc. The urethra runs through the center of the prostate, from the bladder to the penis.(See Figure 1.1) The prostate is surrounded by blood and lymphatic vessels. Blood vessels are part of the

circulatory system, which supply oxygen and nutrients and remove waste from the cells of

the prostate. Lymphatic vessels are part of a large network termed the lymphatic system,

which collect and carry fluid and cells from the tissues of the body. The lymphatic vessels

of the prostate carry lymphatic fluid to a mass of lymph nodes located in the pelvic region.
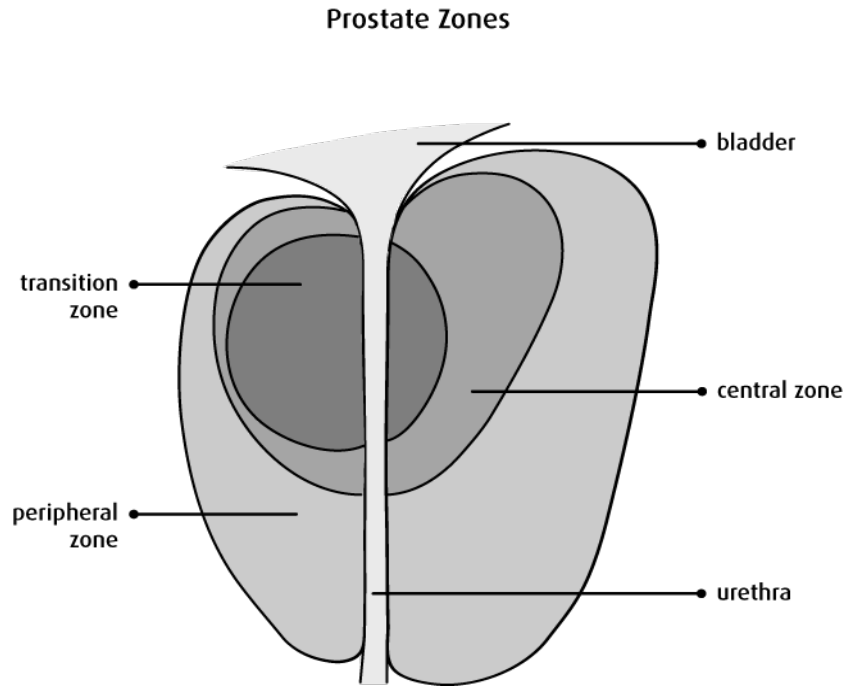
Prostate Zones

Figure 1.2: Zones of the prostate gland. [1]

The prostate gland is divided into three zones: peripheral zone, transition zone, and

central zone. The peripheral zone is the area of the prostate that is closest to the rectum.

It can easily be felt by the doctor during a digital rectal examination (DRE). It is the

largest zone of the prostate gland. The transition zone is the middle area of the prostate,

between the peripheral and central zones. It surrounds the urethra as it passes through

the prostate. This zone makes up about 20% of the prostate gland until the age of 40. As

men age, the transition zone begins to enlarge, until it becomes the largest region of the

prostate. This is called benign prostatic hyperplasia (BPH). When the transition zone enlarges, it pushes the peripheral zone of the prostate toward the rectum. The central zone is in front of the transition zone. It is the part of the prostate that is farthest from the rectum (See Figure 1.2). [1]

1.2.2 Prostate Cancer

Prostate cancer tends to develop in men over the age of fifty. Prostate cancer can be slow-growing and some men who develop prostate cancer may live many years without ever having the cancer detected. It is a disease where some prostate cells have lost normal control of growth and division, and no longer function as normal cells. A cancerous prostate cell might have the features of uncontrolled growth, abnormal structure and the ability to move to other parts of the body (invasiveness). Prostate cancer is associated with urinary dysfunction as the prostate gland surrounds the prostatic urethra (See Figure 1.3). Changes within the gland, therefore, directly affect urinary function. [13]

1.2.3 Prostate Cancer Screening

Screening is the clinical testing leading to finding a disease (e.g. cancer) in people who do not have symptoms of that disease. Screening for prostate cancer aims to find the cancer at an early stage, when it is more curable, and it could be treated more effectively. For a digital rectal exam (DRE), the doctor inserts a gloved, lubricated finger into the rectum to feel for any bumps or hard nodules on the prostate that might be cancer. As shown in the Figure 1.4, the prostate gland is just in front of the rectum, and most cancers begin
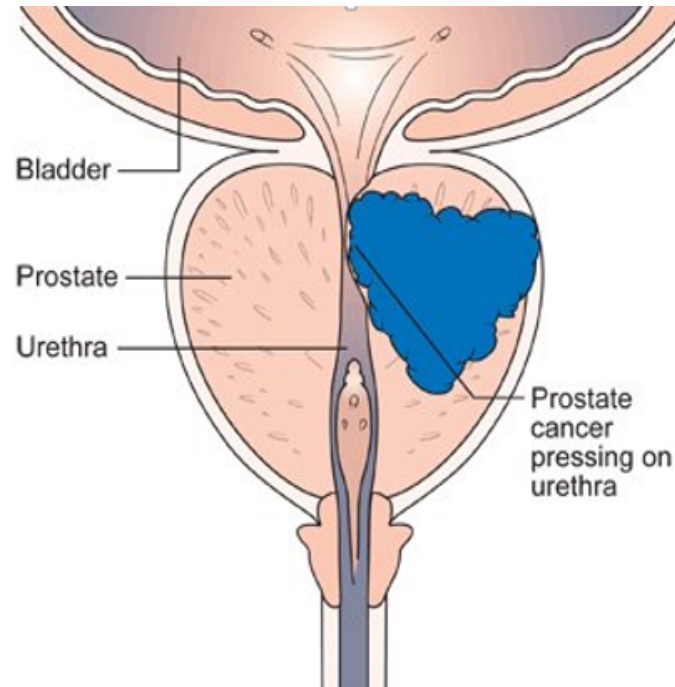
Figure 1.3: Diagram showing prostate cancer pressing on the urethra. [2]

in the anterior part of the gland, which can be felt during a rectal exam. This exam can be uncomfortable (especially in men who have hemorrhoids), but it usually is not painful and only takes a short time. DRE is less effective than the PSA blood test in finding prostate cancer, but it can sometimes find cancers in men with normal PSA levels. For this reason, it may be included as a part of prostate cancer screening. However, it is not sensitive to detecting early-stage small cancers, and is also limited by the physician's access to the prostate posterior. [14]

A prostate-specific antigen (PSA) test is done to measure the level of PSA in the blood. PSA is a protein produced by prostate cells, and abnormal amounts of PSA in the blood may indicate the presence of prostate cancer. If the level of PSA is higher than normal (4 ng/ml), it could be due to a prostate cancer. [15] However, there are also other causes of raised PSA, such as infection, inflammation, an enlarged prostate and
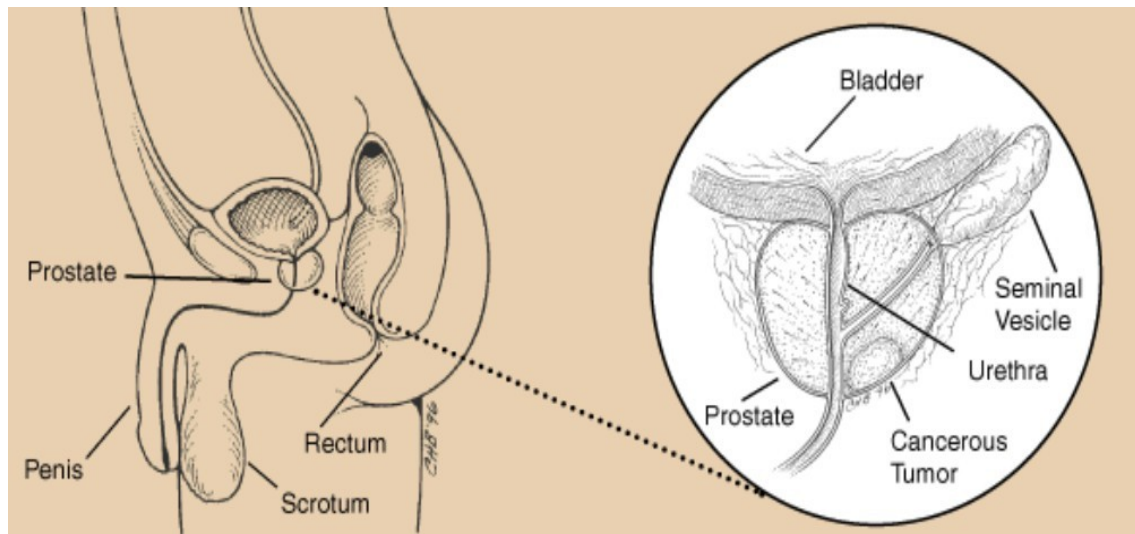
Figure 1.4: Diagram showing the location of most prostate cancers. [2]

even exercise and sex. [14]

A DRE and PSA test can help detect prostate cancer early, but they are not 100% accurate. They can sometimes miss prostate cancer when it is present (false negative) or cause false alarms by suggesting that prostate cancer is present when it is not (false positive). If the result of one of these tests is abnormal, the patient generally requires a biopsy to confirm the diagnosis.

1.2.4 Prostate Cancer Diagnosis Using TRUS Imaging

The standard approach for definitive diagnosis makes use of 2D free-hand TRUS-guided biopsy. Tissue samples are removed for a histological examination during a 2D TRUS-guided biopsy. In most cases, the samples are taken from a pre-determined sextant grid (See Figure 1.5). The number of cores obtained during the biopsy has increased from 6 to 10 or 12 to achieve a satisfactory cancer detection rate. The 12 core transperineal prostate biopsy (See Figure 1.6) provides superior prostate cancer diagnosis to the 6 core

biopsy [16].

The biopsy is performed by inserting an end-firing or side-firing transducer probe into the patients rectum to acquire the ultrasound image of the prostate (See Figure 1.7).
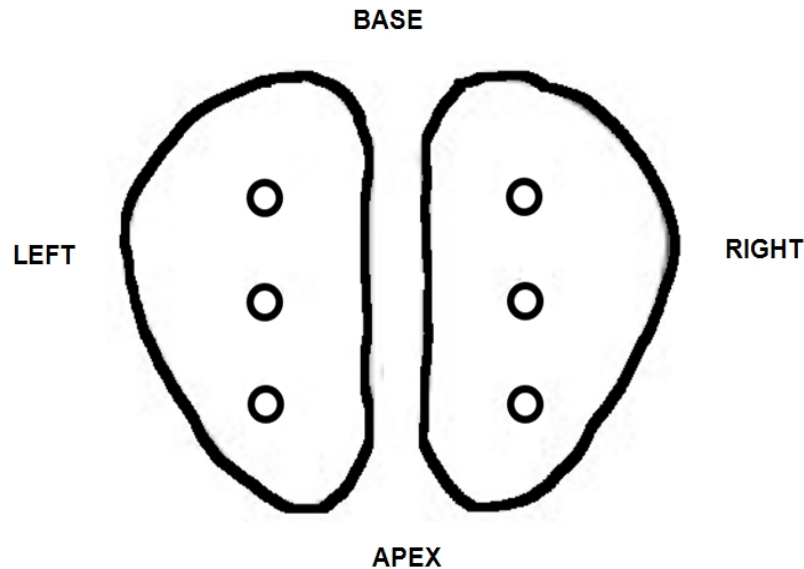
Figure 1.5: Traditional sextant prostate biopsy where a series of six cores are removed.

However, as traditional 2D TRUS images cannot provide the precise 3D position of the biopsy needle, the physician must mentally estimate the 3D location of the biopsy needle based on limited 2D information, which often results in suboptimal biopsy targeting [17].

Multiple 3D TRUS systems have been developed to improve spatial information and permit registration with 3D MR images [18] [19] [20] [21]. We have developed a mechanically-assisted 3D TRUS system [18] that is capable of acquiring a 3D prostate TRUS image in less than 10 s, real time 3D needle guidance and biopsy core 3D spatial recording (See Figure 1.8). Our system allows intra-biopsy fusion of pre-biopsy MRI for the targeted biopsy of suspicious prostate lesions using 3D TRUS needle guidance. This was achieved through a chain of transformations from preoperative MRI to real
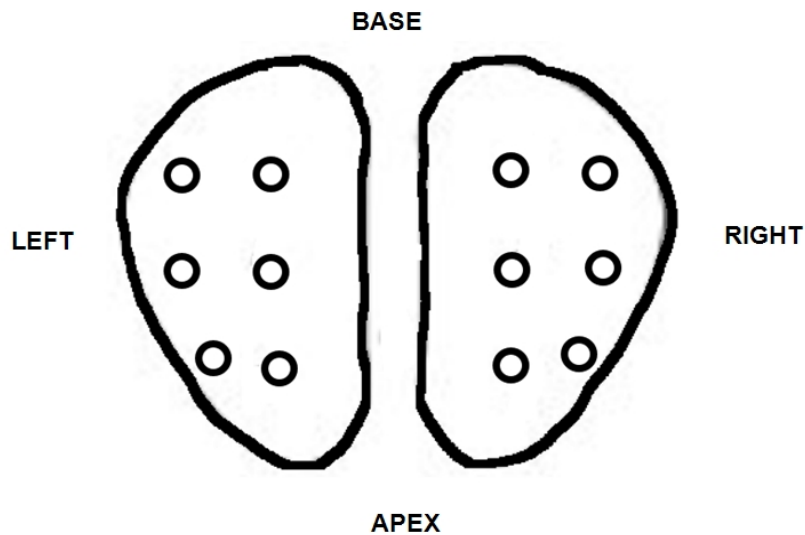
Figure 1.6: Twelve core transperineal prostate biopsy.

time 2D TRUS (see Figure 1.9). The procedure begins with the acquisition of a 3D TRUS image, and multi-parametric MR images, including T2-weighted, dynamic contrast enhanced (DCE) and diffusion-weighted imaging (DWI) MR (See Figure 1.10 for 3D TRUS and T2-weighted MR images). The multi-parametric MR images are used to identify suspicious prostate lesions, and the radiologists finally outline the lesions on the T2-weighted MR image, which is registered to the pre-biopsy 3D TRUS image a few days before biopsy. Preoperative 3D TRUS imaging permits adequate time to ensure proper multimodal registration without prolonging the patient's biopsy procedure or level of discomfort [22]. On the day of the biopsy, a 3D TRUS image is acquired at the start of the biopsy procedure and then this intra-biopsy TRUS image is registered to the pre-biopsy TRUS image to allow for target mapping on the intra-biopsy 3D TRUS [23] [24]. The last step takes place during the biopsy when the registration guides the users to target MR identified lesions, which have been superimposed onto the intra-biopsy image. Any
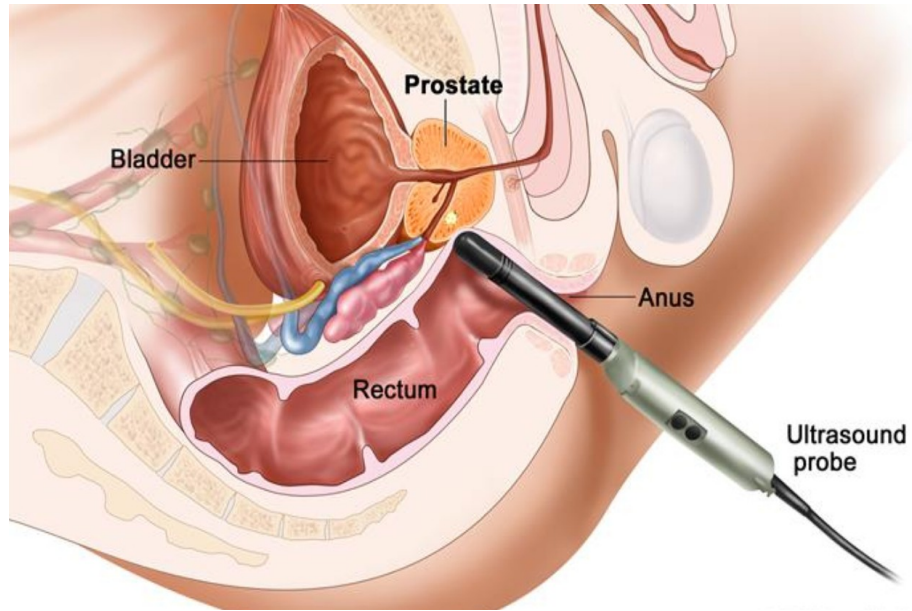
Figure 1.7: An ultrasound probe is inserted into the rectum to acquire images of the prostate. [3]

movement of the prostate is compensated by registering the real time 2D US images with the 3D intra-biopsy TRUS [25].

1.2.5   Prostate Cancer Diagnosis Using MR Imaging

Magnetic resonance imaging (MRI) is accepted as one of the best imaging modalities for detecting and staging prostate cancer due to the excellent anatomical images of the gland that it yields. Reports have shown that multi-parametric MR imaging combined with an endorectal coil can achieve a high degree of accuracy in diagnosing prostate cancer of between 79% - 96% [9] [10] [11]. Generally, T2-weighted imaging has been used for detecting prostate cancer. However, sometimes the diagnostic accuracy of conventional T2-weighted MR is not satisfactory, and recently the use of functional methods, such as DCE, DWI, and spectroscopic imaging, have been recommended as an adjunct to

Figure 1.8: A photograph of the mechanically-assisted 3D TRUS biopsy system with real-time tracking and recording of the 3D position of biopsy needle.

conventional imaging [10]. DCE-MRI can identify early stage prostate cancer with high sensitivity and specificity, and can predict the histological grade to some extent. [26] [27] Combined T2 and DWI MRI is better than T2 imaging alone in the detection of significant cancer within the peripheral zone of the prostate. [28] Studies have also shown that the addition of 3D MR spectroscopic imaging to MR imaging provides better detection and localization of prostate cancer in a sextant biopsy of the prostate than does use of MR imaging alone. [29] [30]
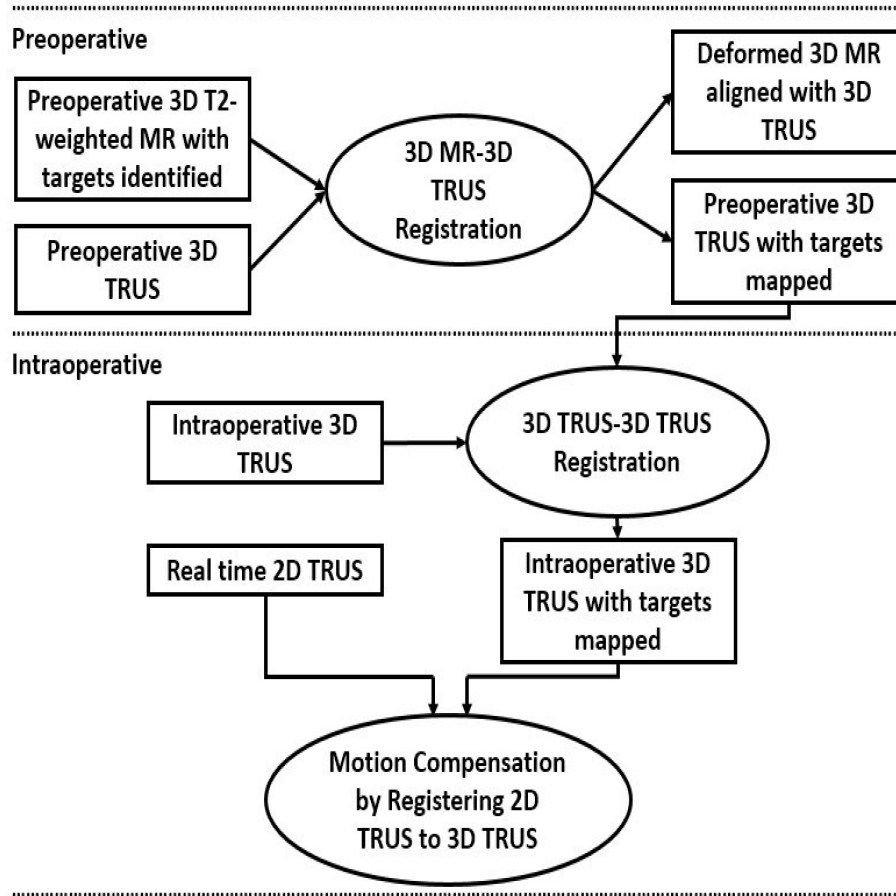
Figure 1.9: Prostate biopsy workflow using our mechanically-assisted 3D TRUS system. [4]

1.3   Registration

1.3.1   3D MR-TRUS Registration for Image-Guided Prostate Biopsy

As our proposed workflow stated in section 1.2.4, with the acquisition of a pre-biopsy 3D TRUS image and multi-parametric MR images, including T2-weighted, DCE and DWI MR. The radiologists identify the suspicious prostate lesions using the multi-parametric MR images, and finally outline the lesions on the T2-weighted MR image. T2-weighted
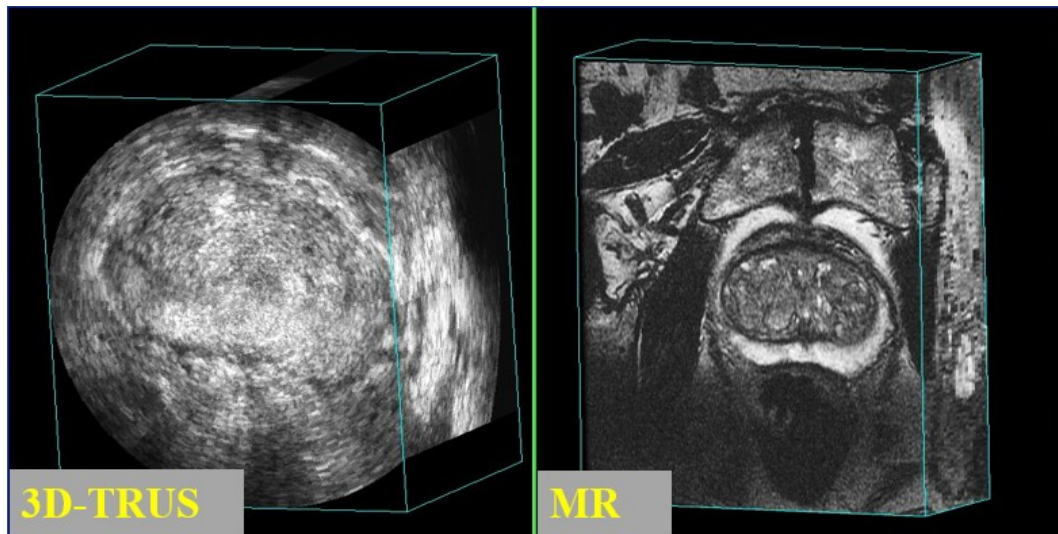
Figure 1.10: 3D TRUS and T2-weighted MR images were required for an MR/3D TRUS-guided biopsy procedure.

MR image is then registered to the pre-biopsy 3D TRUS image, allowing mapping of the identified and outlined suspicious lesions onto the TRUS image.

There is also another clinical workflow, which uses pre-biopsy MR images registerd with the intra-biopsy TRUS directly on the day of the biopsy. [31] The MR images are obtained days, weeks, or even months before the biopsy. On the biopsy day, the operator first collects a series of 2D TRUS images from the prostate base to its apex. After a 3D TRUS prostate volume is reconstructed from the 2D images, the MR and the TRUS images are then spatially aligned with each other.

1.3.2 The Theory of Image Registration

Image registration is the determination of a geometrical transformation that aligns points in one view of an object with corresponding points in another view of that object or another object. [32] The images might be taken at different times and from different
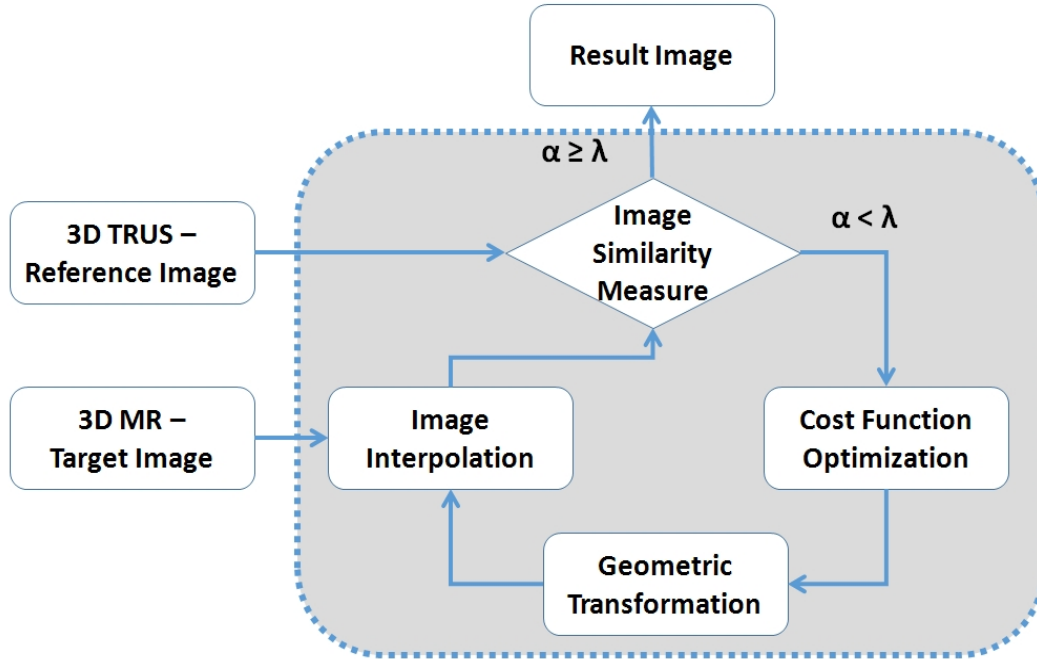
Figure 1.11: A typical image registration schema. This figure is adapted from reference [5].

viewpoints using different imaging modalities. The procedure involves a geometric transformation that includes matching of corresponding points or image features on the images by trying to maximize the similarity between such points or the images while estimating the transformation parameters. A typical image registration algorithm consists of four components: (1) a similarity measure that penalizes the dissimilarity between 2 images; (2) a series of geometric transformations that can be applied to the moving image for the spatially warping step; (3) an optimizer that searches for the optimized transformation that maximizes the similarity; and (4) an interpolator that interpolates image intensities at non-grid locations of the transformed moving image. Figure 1.11 shows a typical image registration framework, where the parameters α and λ represent the matching degree between two temporal images and the preselected threshold, respectively [5].

1.3.3 Image Registration Methods

Geometrical Transformations

(1) Rigid tranformations:

Rigid transformation is defined as a vector space that preserves distances between every pair of corresponding points in the two images to be registered. Two components are used to specify a rigid transformation, a translation and a rotation, which can be formulated as

$$p^{'} = Rp + T \ , \tag{1.1}$$

where, p and $p^{'}$ are the original and transformed images, respectively. R is a 3×3 orthogonal matric defining the rotation portion of the transformation, and T is a 3D vector that may be specified by giving its three coordinates t_x, t_y, t_z relative to a set of x, y, z Cartesian axes.

(2) Non-rigid transformations:

Non-rigid transformations are used not only for non-rigid anatomy, but also inter-patient registration of rigid anatomy or rigid anatomy's intra-patient registration when there are non-rigid deformation during the image acquisition procedure.

Point-Based Methods

A set of corresponding fiducial pairs are selected to specify a transformation that aligns the points. The fiducials are localized by interactive visual identification of anatomical landmarks. Commonly used methods for aligning two sets of corresponding fiducial points involve iterative closest point (ICP) [33] and thin plate spline (TPS) [34]. ICP was

proposed to represent a key approach for registering 3D shapes (including free-form curves and surfaces), which minimizes the distance from the source to the reference point cloud. TPS defines a unique smooth registration from a template image to a target image based on registering corresponding landmarks. It interpolates specified points while minimizing an approximate curvature (integrated squared spatial second derivative).

Surface-Based Method

Surface-based image registration methods involve determining corresponding surfaces in different images (and/or physical space)and computing the tranformation that best aligns these surfaces. [32] The surface representation can be simply a point set (i.e. a collection of points on the surfaces), a faceted surface (e.g. triangle set), an implicit surface, or a parametric surface (e.g. B-spline surface). The methods of aligning two sets of corresponding points on the surfaces are as same as the point-based registration methods mentioned in section 1.3.3.

Intensity-Based Method

The transformation of intensity-based registration is determined by iteratively optimizing the similarity measure, which is calculated from all pixel or voxel values. [32] The optimization part of the registration aims to find the optimal value of the similarity measure.

Intensity-based registration methods can be divided into three classes:

(1) calculating the correlation or sum of differences between two images using the pixel or voxel values alone;

(2) calculating spatial information using pattern intensity, local normalized cross correlation, gradient difference or gradient correlation;

(3) histogram based calculation based on joint entropy or mutual information [35].

1.3.4 Evaluation of Image Registration of the Prostate

As previously stated, accurate 3D MR-TRUS registration is critical for accurate biopsy planning and needle guiding. Target registration error (TRE) [36] [37] indicates the overall misalignment of manually identified corresponding intrinsic fiducials in MR and 3D TRUS prostate images. A target is an anatomical landmark in the patient's prostate that is not used to compute the transformation of the moving image to the fixed image. The set of target points in MR images are denoted as tp_i, and in the TRUS, the corresponding points are tq_i, where $i = 1, ... N$. TRE is defined as the Euclidean distance between a transformed fiducial on the moving and the corresponding fiducial on the fixed images, and the root mean square TRE of all fiducials is given by:

$$TRE = \sqrt{\frac{1}{N} \sum_{i=1}^{N} (T(tp_i) - tq_i)^2} \, , \qquad (1.2)$$

where $T(.)$ is the transformation of the moving image. The fiducials we use for prostate registration are calcifications and cysts, which are manually identified in the MR-TRUS image pairs. Since the TRE is a root mean square error, it gives an estimate of the standard deviation of the normal distribution of biopsy targets given by a registration algorithm, centered on a true target. Such a distribution given by a TRE of 2.5 mm gives a confidence interval corresponding to two standard deviations from the mean in which

95.4% of registered targets are within the 5 mm radius of a clinically significant prostate tumour [23] [38].

The fiducial localization error (FLE) [37] is a statistical measure of the error generated by the variability in locating a fiducial, which allows determination whether fiducial identification dominates the TRE. For FLE determination, the trained operator identifies multiple fiducials (e.g. at least 20 fiducials) in multiple prostate image pairs (e.g. 10 image pairs) multiple times (e.g. 5 times) over several days (e.g. 5 days) and records their coordinates once per day. The variances of the x, y and z coordinates over the five days are then calculated. The FLE for fiducial i is:

$$FLE^i = \sqrt{\sigma^2(X^i) + \sigma^2(Y^i) + \sigma^2(Z^i)} \,, \qquad (1.3)$$

where, X^i, Y^i and Z^i are the sets of x, y and z coordinates of fiducial i selected at different time points. The mean FLE is calculated as:

$$FLE = \sqrt{\frac{1}{N} \sum_{i=1}^{N} (FLE^i)^2} \,, \qquad (1.4)$$

where N =total number of fiducials.

The Dice Similarity Coefficient (DSC) is a measure of overlap between the segmented prostate in transformed moving image (M) and the corresponding segmented prostate in fixed image (F) and is given by:

$$DSC = \frac{2(M \cap F)}{M + F} \qquad (1.5)$$

1.4   Thesis Hypothesis

The central hypothesis of this work is that non-rigid image-based and surface-based MR-TRUS registration methods perform with sufficient accuracy for clinical use in 3D TRUS-guided prostate biopsy. A TRE of less than 2.5 mm indicates clinically acceptble performance. (See section 1.3.4) The specific registration algorithms proposed are: (1) non-rigid image-based 3D MR-TRUS registration using efficient convex optimization, and (2) non-rigid surface-based MR-TRUS registration.

1.5   Thesis Objective

This thesis follows two related objectives, which test the hypothesis stated above. The objective of this work is to develop and evaluate non-rigid image-based and surface-based registration methods for 3D MR-TRUS registraion, allowing identifying and outlining suspicious lesions on MR images, and then mapping onto the TRUS image.

1.6   Thesis Outline

1.6.1   Chapter 2: Non-Rigid Image-Based MR-TRUS Registration

We proposed an image-based 3D MR-TRUS registration method based on a novel duality-based approach for computing the challenging 3D MR-TRUS non-rigid deformable registration fields. A modality independent neighbourhood descriptor (MIND) [39] was used

for similarity metric calculation. A coarse-to-fine scheme was applied to capture large deformations, and at each resolution level, an efficient multiplier-based algorithm was employed to compute an updated incremental deformation field. We validated the proposed registration method on 20 patient 3D MR-TRUS image pairs using TRE, DSC, mean absolute surface distance (MAD) and maximum absolute surface distance (MAXD).

A preliminary work of this chapter has been previously published as a conference paper [40]. A journal version of this chapter with a comprehensive study of the proposed approach, and more experimental validation results has been submitted as, "Three-Dimensional Non-Rigid MR-TRUS Registration Using Dual Optimization," by Y. Sun, J. Yuan, W. Qiu, M. Rajchl, C. Romagnoli, and A. Fenster, to the IEEE Transactions on Medical Imaging, Nov 2013. Manuscript#2013-0816.

1.6.2   Chapter 3: Non-Rigid Surface-Based MR-TRUS Registration

We developed a surface-based non-rigid prostate registration of 3D TRUS to T2-wieghted MR images based on specific prostate boundary point correspondences followed by a 3D TPS deformation. The primary contributions of this paper are: 1) 2D slice correspondences are determined by rotationally re-slicing two segmented prostate surfaces from both 3D MR and TRUS images around a specified rotational axis, which is started by initializing 3 pairs of corresponding anatomical landmarks, and 2) a method for finding the point correspondences based on the resliced 2D corresponding slices. This approach takes into account the correspondences on the prostate surface, inside the prostate, as

well as the centroid of the prostate.

We measured TRE as an indication of the overall misalignment of manually identified corresponding intrinsic fiducials in the MR and 3D TRUS images for 17 image pairs. We also measured the TRE of fiducials within the peripheral zone (PZ) separately, known to be the most common site harboring cancer and subject to deformation caused by the US transducer during biopsy. We measured the FLE to allow determination whether fiducial identification dominated the TRE. For FLE determination, the trained operator identified 30 fiducials in 10 prostate image pairs (three fiducials/prostate) five times over five days and recorded their coordinates once per day.

A preliminary work of this study has been published as a conference paper, [41] and an extended journal version with the registration approach altered and improved is about to be submitted to Medical Physics.

Chapter 2

Non-Rigid Image-Based MR-TRUS Registration

2.1 Introduction

Few image-based registration methods to date have contributed to image-based 3D MR-TRUS prostate registration. Mutual information (MI) for image-based multi-modal registration methods was first introduced by Maes *et al.* [42]. They aimed to find a statistical intensity relationship across images, thereby maximizing the amount of shared information between two images. Heinrich *et al.* [39] proposed a modality independent neighborhood descriptor (MIND) for multi-modal deformable registration. They made use of the concept of local self-similarity within small image patches of one image and aimed to extract the distinctive structure in a local neighborhood that is preserved across modalities.

Strong clinical interests motivate the development of efficient 3D MR-TRUS registra-

22

tion methods that dictate fewer interactions to decrease operator variability, especially the variational optical-flow based optimization approaches [43], which rely on a fast numerical solver to the defined nonlinear optimization problem. For the studied image-based non-rigid medical image registration problems, much attention has been given to the Horn & Schunck scheme [44] [45] combined with an incremental coarse-to-fine strategy. It can properly compute a non-rigid deformation field with sufficient smoothness and capture substantial deformations. In particular, a partial differential equation (PDE) diffusion-based algorithm is often derived as the first-order solver due to its simplicity in implementation. However, only a local optimum can be obtained, and the numerical scheme also requires the diffusion step-size to be small enough to achieve convergence, for which more diffusion iterations are needed. A convex optimization method was recently successfully developed to solve a wide spectrum of problems in image processing [46] [47]. It provides both a sound analysis in mathematics and efficient algorithm in computation, with the capability of tackling the non-smooth image matching terms and deformation regularization functions.

This chapter describes an image-based 3D MR-TRUS registration method based on a novel duality-based approach for computing the challenging 3D MIND-based non-rigid deformable registration fields. A coarse-to-fine scheme was applied to capture large deformations, and at each resolution level, an efficient multiplier-based algorithm was employed to compute an updated incremental deformation field. We validated the proposed registration method on 20 patient 3D MR-TRUS image pairs using target registration error (TRE), Dice similarity coefficient (DSC), mean absolute prostate surface distance (MAD) and maximum absolute surface distance (MAXD).

2.2   Methods and Experiments

The MIND method introduced by Heinrich *et al.* [39] presented an image descriptor independent of the modality, contrast and noise that remained sensitive to inherent image features such as image corners or edges, etc. The method is based on the local image self-similarity feature, which was originally introduced by Buades *et al.* [48] for image denoising. Heinrich *et al.* [39] demonstrated that in terms of image registration, especially when dealing with different image modalities, a point-wise MIND descriptor performs better than other proposed image information descriptors, such as normalized mutual information (NMI) [49] or patch-based entropy descriptor [50]. We utilized MIND as the cross-modality measure to the 3D non-rigid MR-TRUS deformable registration (See Figure 2.1). Let $I^M(x)$ and $I^R(x)$ be the input 3D MR and TRUS images
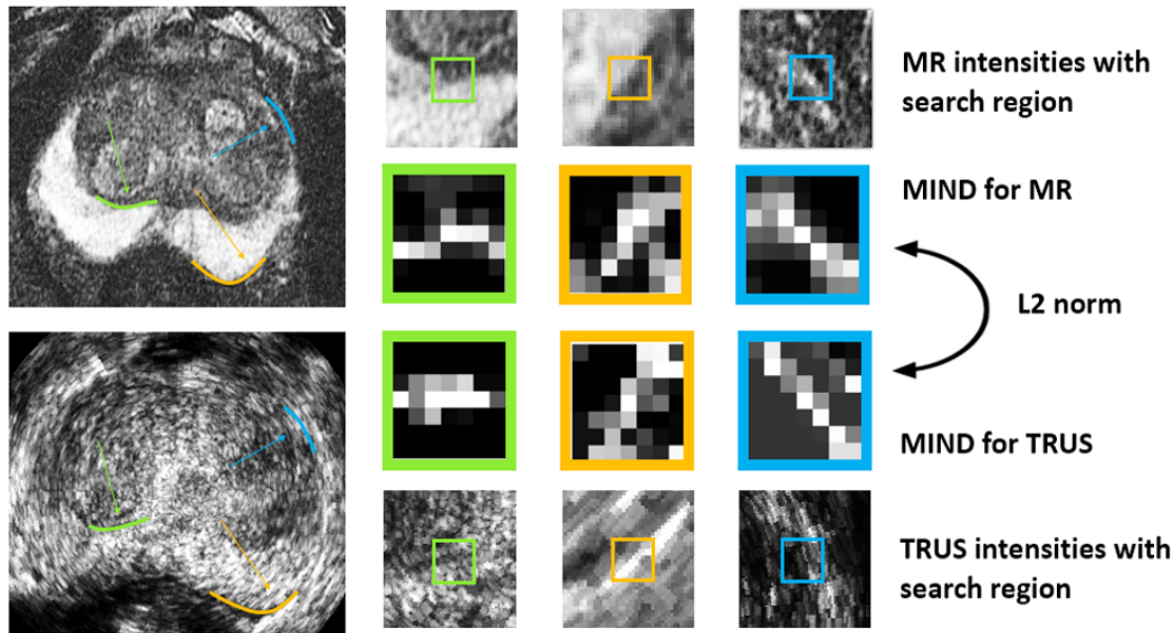
Figure 2.1: Proposed concept for the use of MIND for multi-modal registration. MIND is calculated for each voxel in the MR and 3D TRUS images.

respectively. $\mathcal{M}(x) := (m_1(x), \ldots, m_k(x))^{\mathrm{T}}$ and $\mathcal{R}(x) := (r_1(x), \ldots, r_k(x))^{\mathrm{T}}$ be the computed k-channel MIND descriptor at x associated with the MR image $I^M(x)$ and the TRUS image $I^R(x)$, where k is the dimension of the applied MIND descriptor. We aim to minimize a difference measure between $\mathcal{M}(x)$ and the deformed $\mathcal{R}(x + u)$ over the deformation field $u(x) = (u_1(x), u_2(x), u_3(x))^{\mathrm{T}}$, which can be essentially formulated as

$$\min_{u} \ P(u) := \sum_{i=1}^{k} \int p_i(m_i(x) - r_i(x + u)) \, dx \,, \tag{2.1}$$

where the penalty function $p_i(v)$, $i = 1 \ldots k$, is often positive and convex. For example, when $p_i(v) = |v|^2/2$, $i = 1 \ldots k$, the above formulation defines the sum of squared difference measure (SSD). Clearly, the minimization of (2.1) is ill-posed, for which a smoothness regularization of the deformation field $u(x)$ is often added to (2.1) to restrict the solution space of $u(x)$.

In this method, the convex regularization term is considered as $G(u) := \sum_{i=1}^{3} \int |\nabla u_i|^2 \, dx$, which results in the following minimization problem

$$\min_{u} \ P(u) + \frac{\alpha}{2} \sum_{i=1}^{3} \int |\nabla u_i|^2 \, dx \,, \tag{2.2}$$

where $\alpha > 0$ is a constant.

2.2.1   Incremental Gauss-Newton and Primal-Dual Optimization

Note the MIND-difference term $P(u)$ in (2.2) is often highly non-linear, hence the energy function of (2.2). To efficiently address the challenging minimization problem of (2.2), a nonlinear Gauss-Newton optimization scheme is applied [51]. It results in a series of incremental Horn-Schunck warping steps [51], where each step properly approximates an update $h(x) = (h_1(x), h_2(x), h_3(x))^{\mathrm{T}}$ to the current deformation estimation $u(x)$, till the updated deformation $h(x)$ is sufficiently small.

In particular, the incremental deformation $h(x)$ at each updating step is estimated by solving the following optimization problem:

$$\min_{h} \frac{1}{2} \int (P_0 + \nabla P \cdot h)^2 dx \, + \, \frac{\alpha}{2} \sum_{i=1}^{3} \int |\nabla(u_i + h_i)|^2 \, dx \,, \tag{2.3}$$

where the highly nonlinear function $P(u)$ of (2.2) is linearized and penalized by its convex quadratic function.

Clearly, (2.3) amounts to a convex optimization problem. In this work, we study such convex minimization problem (2.3) based upon a novel primal-dual framework, which not only provides a mathematical dual analysis on (2.3) but also derives a new dual optimization algorithm.

In fact, with help of the equivalent conjugate representations of convex functions, we can derive its mathematically equivalent formulation, i.e. the *dual model*, to the convex minimization problem (2.3) by the modern convex optimization theories, such that

Proposition 2.2.1 *The* convex minimization problem (2.3) *can be equally represented by its* dual model*:*

$$\max_{w,q} E(w,q) := \int (wP_0 + \sum_{i=1}^{3} u_i \operatorname{div} q_i)dx - \frac{1}{2}\int w^2 dx \qquad (2.4)$$

$$- \frac{1}{2\alpha}\sum_{i=1}^{3}\int q_i^2(x)dx$$

subject to

$$F_i(x) := (w \cdot \partial_i P + \operatorname{div} q_i)(x) = 0\,; \qquad (2.5)$$

for $\forall x \in \Omega$, *where* $i = 1, 2, 3$.

Its proof is given in APPENDIX A.1.

2.2.2 Dual Optimization Algorithm

As in Sec. A.1, each component of the incremental deformation field $(h_1(x), h_2(x), h_3(x))^\mathrm{T}$ just works as the multiplier function to the respective linear equalities (2.5) under the perspective of primal and dual. To this end, the energy function of the primal-dual model (A.5) (See APPENDIX A.1) just gives the Lagrangian function to the *dual formulation* (2.4), i.e.

$$L(h,w,q) = \int (wP_0 + \sum_{i=1}^{3} u_i \operatorname{div} q_i)dx - \frac{1}{2}\int w^2 dx$$

$$- \frac{1}{2\alpha}\sum_{i=1}^{3}\int q_i^2 dx + \sum_{i=1}^{3} \langle h_i, F_i \rangle\,, \qquad (2.6)$$

where the linear functions $F_i(x)$, $i = 1, 2, 3$, are given in (2.5). Then, we define its augmented Lagrangian function

$$L_c(h, w, q) = L(h, w, q) - \frac{c}{2} \sum_{i=1}^{3} \|F_i\|^2 \,, \tag{2.7}$$

where c is a positive constant and the additional quadratic penalty function is applied to force the linear equalities (2.5).

Therefore, we can derive an efficient duality-based Lagrangian augmented algorithm, see [52, 53, 46] for details:

- Set the staring values of w^0, q^0 and h^0, and let $k = 0$;

- Fix q^k and h^k, optimize w^{k+1} by

$$w^{k+1} := \arg\max_w \, L_c(h^k, w, q^k) \,. \tag{2.8}$$

It generates the following convex minimization problem:

$$\min_w \frac{1}{2} \int (w - P_0)^2 dx + \frac{c}{2} \sum_{i=1}^{3} \int (w\partial_i P - T_i^k)^2 dx \,; \tag{2.9}$$

where $T_i^k(x)$, $i = 1\ldots 3$, are fixed. Therefore, w^{k+1} can be simply computed by

$$w^{k+1} = \frac{P_0 + c\sum_{i=1}^{3}(\partial_i P \cdot T_i^k)}{1 + c\sum_{i=1}^{3}(\partial_i P)^2} \,. \tag{2.10}$$

- Fix w^{k+1} and h^k, optimize q^{k+1} by

$$q^{k+1} := \arg\min_q \; L_c(h^k, w^{k+1}, q) \, ; \tag{2.11}$$

which gives the following three convex minimization problems:

$$\min_{q_i} \; \frac{1}{2\alpha} \int (q_i + \alpha \nabla u_i)^2 dx + \frac{c}{2} \int (\operatorname{div} q_i - U_i^k)^2 dx \, , \tag{2.12}$$

$i = 1\dots 3$; where U_i^k, $i = 1\dots 3$, are fixed. Hence, q_i^{k+1}, $i = 1\dots 3$, can be simply computed by gradient descent.

- Update h^{k+1} by

$$h_i^{k+1} = h^k - c\Big(w^{k+1} \cdot \partial_i P + \operatorname{div} q_i^{k+1}\Big) \, ; \quad i = 1, 2, 3 \, ; \tag{2.13}$$

- Set $k = k + 1$ and iterate the above three steps till convergence, i.e.

$$c \left\| w^{k+1} \cdot \partial_i P + \operatorname{div} q_i^{k+1} \right\| \leq \delta \, , \tag{2.14}$$

where δ is a chosen small positive parameter (5×10^{-4}) to determine convergence and $\|\cdot\|$ is the L1-norm defined as below:

$$\|g(x)\| = \int |g(x)| \, dx \, . \tag{2.15}$$

2.2.3   Coarse-to-Fine Incremental Scheme

A coarse-to-fine scheme is applied to capture large deformations. First, we construct a coarse-to-fine pyramid of each MIND descriptor function: let $\mathcal{M}^1(x) \ldots \mathcal{M}^L(x)$ be the L-level coarse-to-fine pyramid representation of $\mathcal{M}(x)$ from the coarsest resolution $\mathcal{M}_1(x)$ to the finest resolution $\mathcal{M}^L(x) = \mathcal{M}(x)$; and $\mathcal{R}^1(x) \ldots \mathcal{R}^L(x)$ the L-level coarse-to-fine pyramid representation of $\mathcal{R}(x)$.

At each ℓ level, $\ell = 1 \ldots L$, we compute the deformation field $u^\ell(x)$ based on the two MIND functions $\mathcal{M}^\ell(x)$ and $\mathcal{R}^\ell(x + u^{\ell-1})$ at the same resolution level, where $\mathcal{R}^\ell(x + u^{\ell-1})$ is warped by the deformation field $u^{\ell-1}(x)$ computed at the previous level $\ell - 1$. For the coarsest level, i.e. $\ell = 1$, the so-called previous-level deformation is set to be 0. In our implementation $L = 4$.

2.2.4   Experiments

This study was conducted with images acquired with the approval of the institutions Human Subjects Research Ethics Board and with the informed consent of all subjects. The proposed convex optimization approach to non-rigid MR-3D TRUS registration was implemented using parallel computing architecture (CUDA, NVIDIA Corp., Santa Clara, CA), and the user interface was developed in Matlab (Natick, MA, USA). The experiments were conducted on a Windows desktop with an Intel i7-3770 CPU (3.4 GHz) and a GPU of NVIDIA Geforce 680GTX. The mean computation time was calculated by running the program for 10 patients.

Materials

T2-weighted MR images were acquired using a body coil and corresponding 3D TRUS images from 20 patients scheduled prostate biopsy. The MR images were obtained using a whole-body 3.0-T Excite 12.0 MRI system (GEHC, Milwaukee, WI, USA) at an image size of $512 \times 512 \times 36$ voxels with a voxel size of $0.27 \times 0.27 \times 2.2$ mm^3. The 3D TRUS images were acquired using a 3D TRUS mechanical scanning system developed in our laboratory [18], using a Philips HDI-5000 US machine with a Philips end-firing C9-5 transducer (Philips, Bothell, WA, USA). The 3D TRUS image size was $448 \times 448 \times 350$ voxels with a voxel size of $0.19 \times 0.19 \times 0.19$ mm^3.

Manual Initialization

We initialized the registration to generate a rigid transform as an initial approximate alignment using six manually placed approximately corresponding landmarks: leftmost, rightmost, topmost, bottommost points on the largest view of the prostate axial slices [54]; the urethra at its entrance into the prostate; and the end point of the peripheral zone at the apex on the 3D TRUS and MR images. These approximately selected landmarks, such as on the prostate boundary and bladder, are geometric features that can be identified on both modalities. The MR image was then resampled to have the same dimensions and voxel size as the TRUS image. Figure 3.1 shows an example of six operator selected landmarks on the prostate boundary. Figure 3.1(b) shows the selection on the axial MR and 3D TRUS slices, corresponding to the 2D image with the largest view of the prostate, Figure 3.1(c) at the urethra's entrance point into the prostate, and Figure 3.1(a) at the
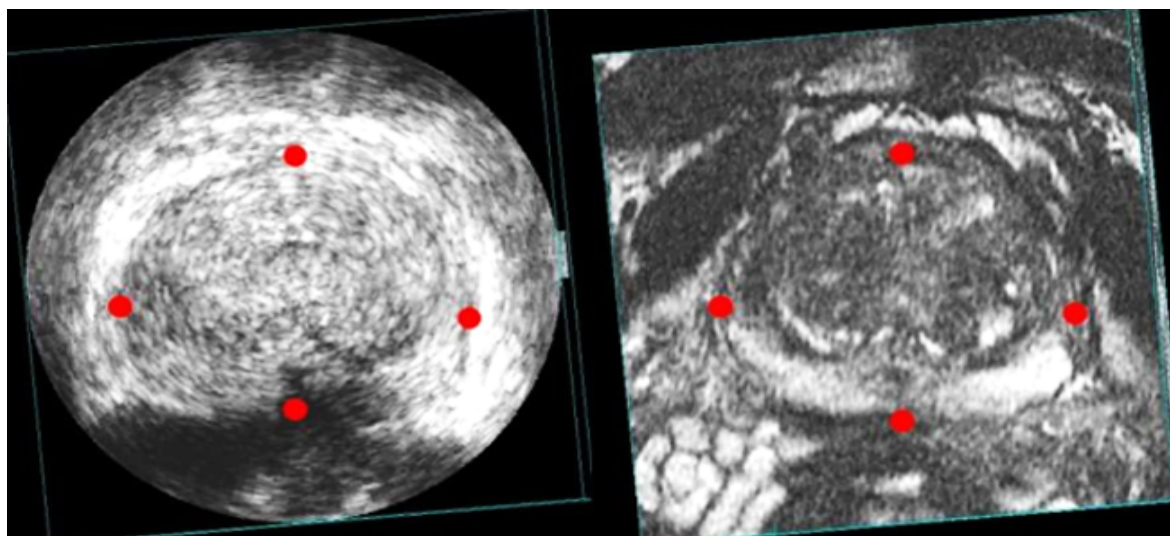
(a)
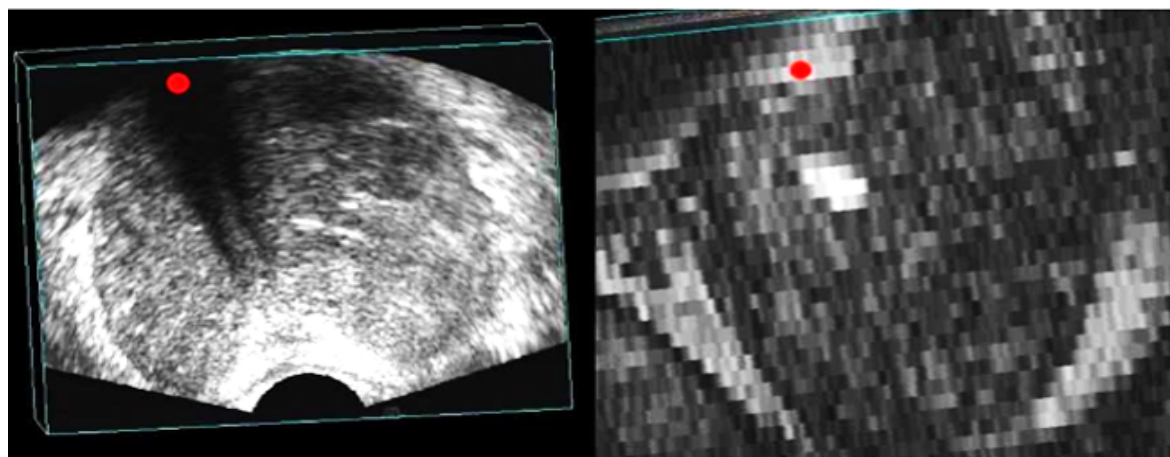
(b)
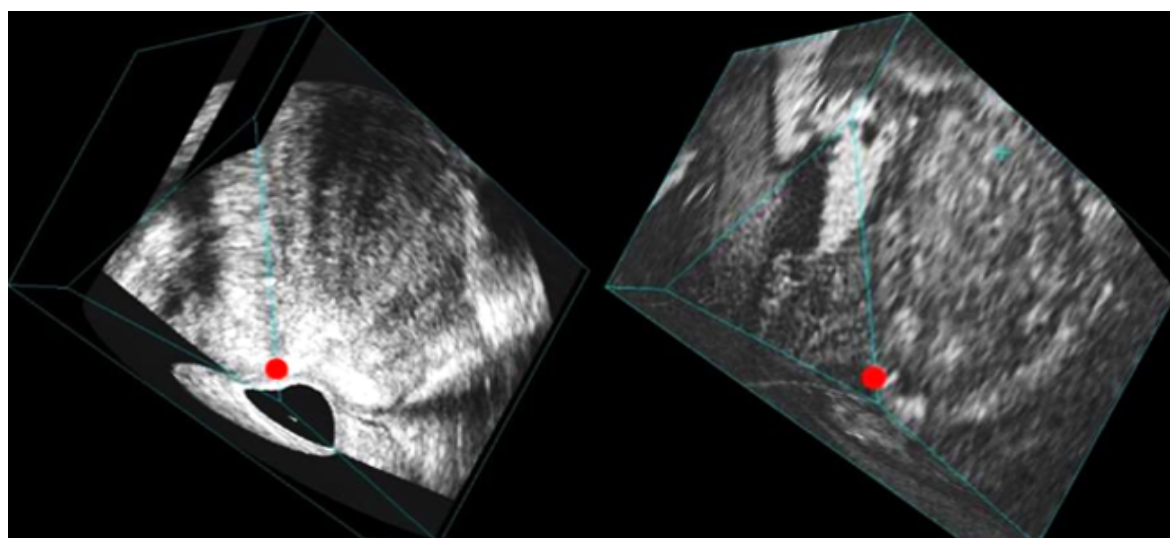
(c)

Figure 2.2: Red dots indicate approximate corresponding anatomical landmarks on 3D TRUS images (left column) and MR (right column), (a) shows the corresponding left-most, rightmost, topmost, bottommost points on the largest view of the axial slices, (b) shows the corresponding entrance points of urethra into the prostate, and (c) shows the corresponding end points of peripheral zone at the apex.

end of the peripheral zone of the apex.

2.2.5   Evaluation

Accuracy

We measured the target registration error (TRE) [36] [37] as the overall misalignment of manually identified corresponding intrinsic fiducials in MR and 3D TRUS images. The approximate corresponding landmarks used for initialization were not used in the evaluation. Seventy-nine fiducials (calcifications / cysts) were manually identified in the twenty image pairs by a trained operator (Y.S.) under the supervision of an experienced radiologist (C.R.). Of the 79 fiducials selected, 27 were within the peripheral zone (PZ), known to be the most common site harboring cancer [55] and subject to deformation caused by the US transducer during biopsy. Accurate biopsy targeting relies on corrections being made for this deformation. We also measured the fiducial localization error (FLE) [37] to allow determination whether fiducial identification dominated the TRE. For FLE determination, the trained operator identified 30 fiducials in 10 prostate image pairs (three fiducials/prostate) five times over five days and recorded their coordinates once per day. In addition, we measured the TRE dependence on fiducial distance from the probe tip to determine our ability to correct the deformation induced by the TRUS transducer.

The trained operator manually segmented prostate surfaces from both MR and 3D TRUS images under the supervision of an experienced radiologist (C.R.). Using the segmented prostate boundaries, we compared the registered MR and corresponding 3D

TRUS images by calculating the DSC [56], MAD, and MAXD [57]. All validation metrics were separately calculated for three prostate sub-regions: the apex, mid-gland and base, selected along the apex-base axis of the manual segmented TRUS prostates (0.3, 0.4, 0.3 of the length of the apex-base axis respectively) [54]. A slice-by-slice DSC calculation was also performed, which aims to investigate the overlap between 2D slices of MR and TRUS images from apex to base. We first found the two end points of the apex and base from an axial view of a prostate, and then equidistantly extracted 10 slices between the two points along the apex-base axis. Thus we were able to calculate the DSC for the 10 slices. Figure 2.3 shows an example of the extracted slices (slice number 2, 4, 6 and 8, labeled from the apex) of a prostate.

Statistical analyses were performed in SPSS Version 15.0 (SPSS, Chicago, IL) to determine if there was a significant difference in the TREs between the manual rigid initialization and deformable registration.

Reproducibility

The variability of our registration method was determined by calculating the dependence of the non-rigid registration on the manual rigid initialization. To study the effects of variability of selecting approximate fiducials during initialization on TRE, 10 patients' 3D prostate MR-TRUS image pairs were selected. These 3D MR-TRUS images were initialized using manually identified fiducials selected by three trained operators, five times each. Each initialization procedure was performed at least one day after the previous session in order to minimize learning effects. The initialized MR-TRUS images were then used for non-rigid registration. TRE values for each trial and the overall TRE for all
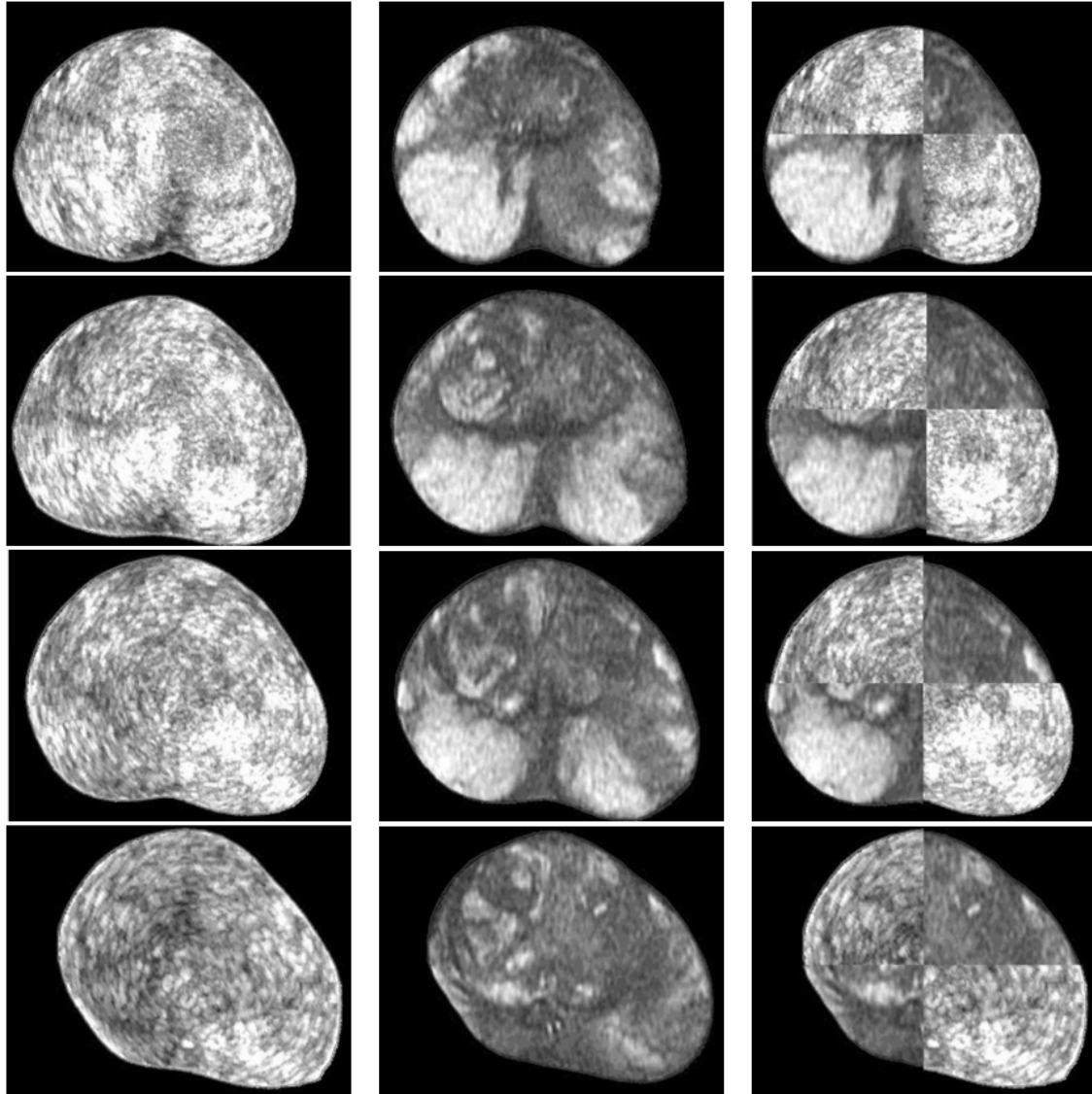
Figure 2.3: Columns 1 and 2 show fixed TRUS and registered MR images respectively. Column 3 shows the checkerboard of our proposed registration method. The rows show the apex to base registration results slice-by-slice from top to bottom. The slices from one prostate are slice 2, 4, 6 and 8 labeled from the apex.
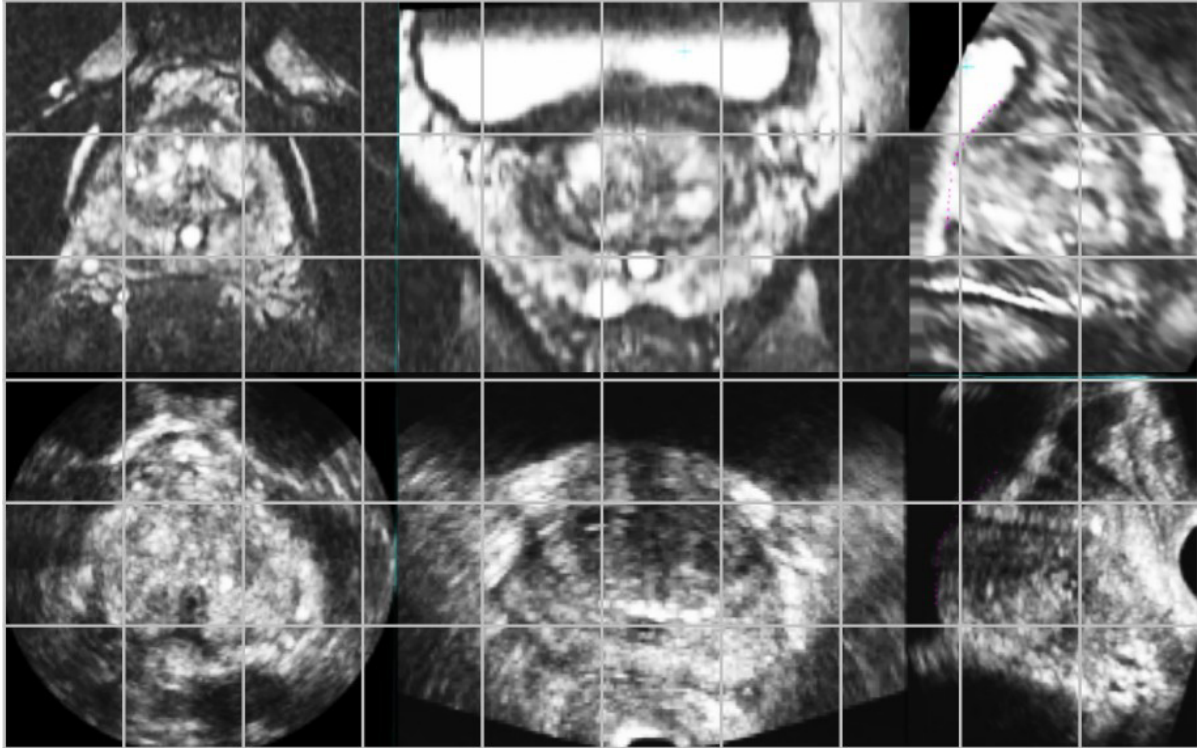
Figure 2.4: Examples of axial (left column), coronal (middle column) and sagittal (right column) views through registered MR (top row) and 3D TRUS (bottom row) images.

patients were then calculated.

2.3   Results

2.3.1   Accuracy

Figure 2.4 shows examples of registered MR and 3D TRUS images from axial, coronal and sagittal views. The median and mean TRE results for the initial rigid alignment and the non-rigid registration are summarized in Table 2.1, which shows an overall mean TRE of 3.37 ± 1.23 mm for the rigid initialization and 1.93 ± 0.73 mm for the non-rigid registration.

We performed a Shapiro-Wilk test on the TREs calculated for the initial rigid trans-

Table 2.1: TREs for 20 patient image pairs.

Patient#	Rigid RMS TRE (mm)		Non-rigid RMS TRE (mm)	
	Median	Mean $\pm$ std	Median	Mean $\pm$ std
1	2.76	2.76 ± 0.25	2.49	2.41 ± 0.58
2	2.47	2.25 ± 0.61	1.32	1.31 ± 0.22
3	2.06	2.17 ± 0.58	1.61	1.83 ± 0.54
4	1.96	2.19 ± 0.47	1.15	1.65 ± 1.06
5	2.29	2.30 ± 0.33	1.26	1.31 ± 0.69
6	2.30	2.25 ± 0.32	1.47	1.47 ± 0.03
7	1.70	1.69 ± 0.27	1.11	1.13 ± 0.27
8	1.54	1.74 ± 0.44	0.81	1.01 ± 0.35
9	3.30	3.74 ± 0.67	2.97	2.89 ± 0.12
10	3.15	2.92 ± 0.56	2.17	1.96 ± 0.40
11	5.44	5.49 ± 0.72	1.87	1.96 ± 0.79
12	3.22	3.28 ± 0.27	2.25	2.32 ± 0.18
13	2.88	3.11 ± 0.69	1.14	1.66 ± 0.77
14	3.32	3.32 ± 0.30	1.56	1.90 ± 0.86
15	4.29	4.24 ± 0.27	2.05	2.22 ± 0.54
16	3.68	4.17 ± 1.10	2.12	2.27 ± 0.26
17	5.70	5.76 ± 0.11	1.96	1.88 ± 0.28
18	3.13	3.16 ± 0.77	1.79	1.90 ± 0.79
19	4.35	4.21 ± 0.63	2.31	2.40 ± 0.39
20	4.83	4.88 ± 0.09	1.05	1.60 ± 0.75
All	2.95	3.37 ± 1.23	1.76	1.93 ± 0.73

Table 2.2: TREs for peripheral zone (PZ), central gland (CG) and whole gland (WG).

	PZ	CG	WG
# of fiducials	27	52	79
Mean (mm)	1.97 ± 0.67	1.90 ± 0.76	1.93 ± 0.73
Median (mm)	1.80	1.75	1.76

form and deformable registration data sets (see Table 2.1). This test revealed the TRE distributions of manual rigid initialization and deformable registration were both non-normal ($p < 0.05$). Thus, we performed a Wilcoxon Sign Rank test for non-normal

Table 2.3: Results of DSC for the prostate apex, mid-gland and base, and MR-TRUS surface distance metrics.

Patient#	DSC (%)				Surface distance (mm)	
	Apex	Mid	Base	WG	MAD	MAXD
1	83.7	94.9	85.5	91.2	1.38	5.95
2	78.0	92.7	81.5	90.7	1.30	3.78
3	82.1	88.2	78.7	87.3	1.63	6.91
4	87.7	92.1	76.0	90.9	1.08	4.85
5	85.2	92.3	70.7	85.2	1.64	6.83
6	83.1	95.6	84.8	87.7	1.59	7.14
7	82.3	90.6	78.7	90.2	1.04	4.85
8	84.5	89.4	76.6	85.4	1.73	8.26
9	89.8	95.0	79.0	83.9	2.25	12.84
10	72.6	89.7	80.5	79.2	2.43	7.63
11	61.2	83.0	70.0	77.6	2.75	8.76
12	84.6	93.5	91.7	82.9	2.13	7.92
13	90.2	94.4	84.7	91.8	1.45	4.60
14	86.0	95.4	92.4	85.9	1.83	5.91
15	77.1	87.6	73.6	85.6	1.58	8.95
16	88.1	93.8	82.4	86.0	2.04	5.57
17	80.8	95.4	88.7	85.4	2.24	6.27
18	83.1	94.8	88.3	89.5	1.49	5.38
19	67.2	92.8	85.9	84.1	2.29	6.49
20	69.0	88.4	84.1	74.2	2.91	9.07
All	80.8 ± 7.8	92.0 ± 3.4	81.7 ± 6.4	85.7 ± 4.7	1.84 ± 0.52	6.90 ± 2.07

distributions, which indicated a significant difference between the TRE values of the two study groups, ($p < 0.01$).

The FLE was 0.21 mm for 3D TRUS images, and 0.18 mm for MR. Thus, the FLEs did not dominate the overall TRE. The mean and median TRE values for PZ, central gland (CG) and whole gland (WG) are summarized in Table 2.2, which shows that the mean TRE for PZ is about 0.1 mm higher than the value for CG.

Figure 3.5(a) shows the frequency distribution of all measured TREs of the initial rigid
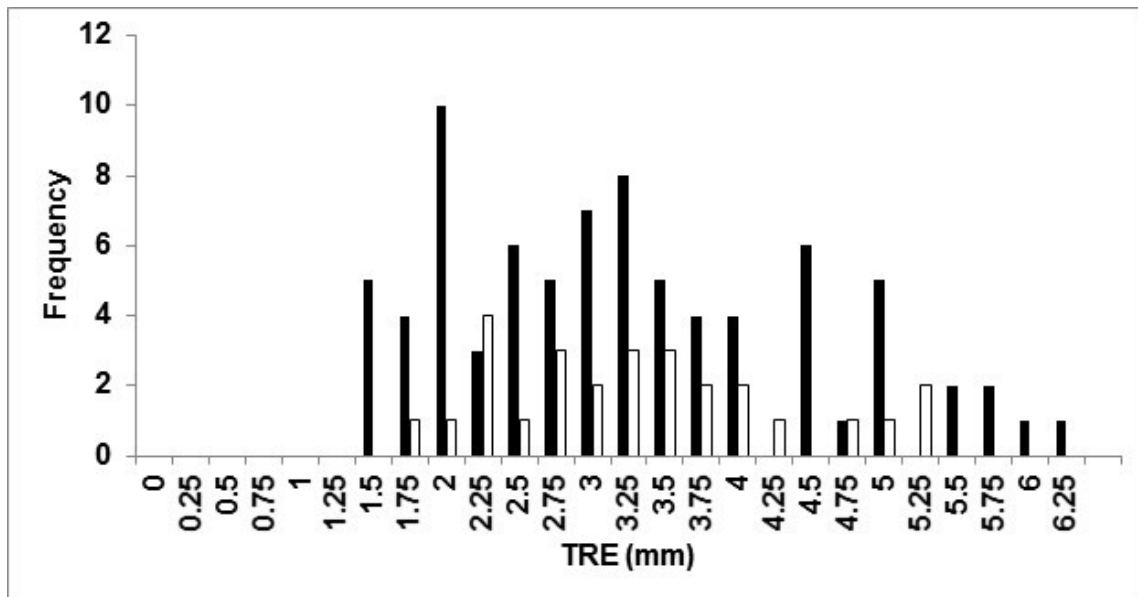
(a)
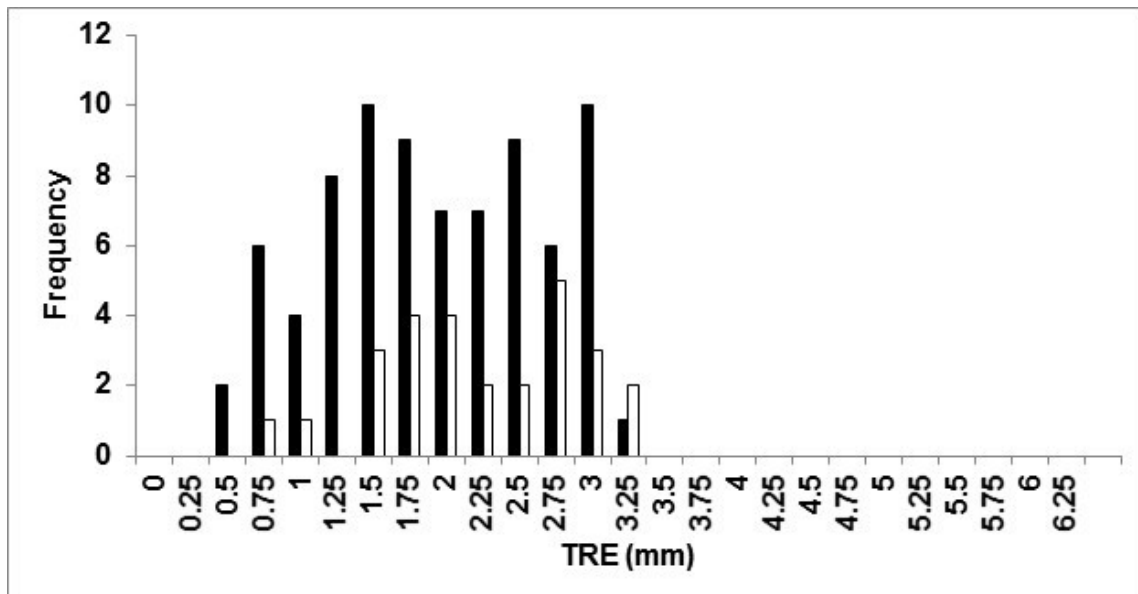
(b)

Figure 2.5: Whole gland (WG) (black) and peripheral zone (PZ) (white) frequency distributions of: (a) initial alignment TRE between all 79 fiducial pairs, and (b) non-rigid registration TRE.
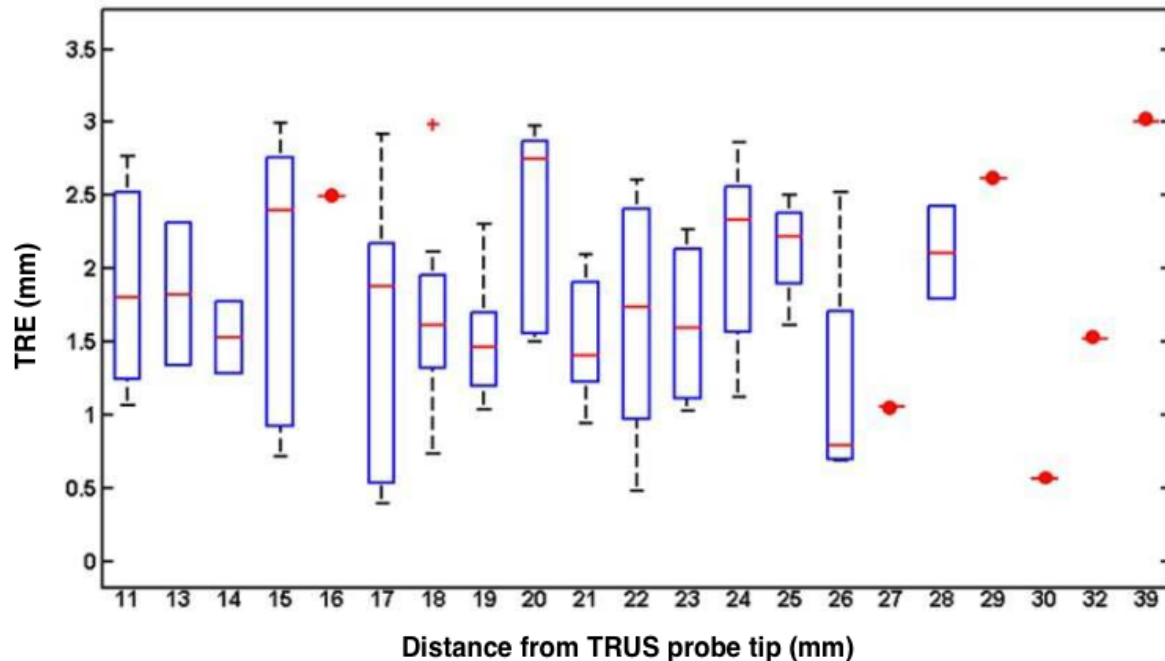
Figure 2.6: Plots of the spatial distribution of TREs: The TREs are plotted against the Euclidean distance (mm) from the TRUS probe tip with distance bin range of 1 mm. (The central red marks are the medians; the edges of the boxes show the 25th and 75th percentiles; the whiskers extend to the most extreme data points not considered outliers; the one outlier is plotted as a plus sign individually, and the distance bin with only one fiducial is plotted as a red dash with a red dot. The range of the distances are based on the ability to find fiducials and size of prostate.)

alignment and Figure 3.5(b) the non-rigid registration for the WG and PZ. Figure 3.5(b) shows that 78% of the TRE values for WG and 63% for PZ are below a value of 2.5 mm. The TREs as a function of fiducial distance from the transducer tip are plotted in Figure 2.6, which indicates that there is little dependence of the TRE values on the fiducial distance from the transducer probe tip.

Table 2.3 shows the mean DSC, MAD and MAXD for WG, apex, mid-gland, and base, respectively. It shows an average DSC of $80.8 \pm 7.8\%$ for the apex of the prostate, $92.0 \pm 3.4\%$ for the mid-gland, $81.7 \pm 6.4\%$ for the base and $85.7 \pm 4.7\%$ for the whole gland. The results of surface distance calculation show an overall average of 1.84 ± 0.52

Table 2.4: Results of slice-by-slice DSC (%) per slice for 10 slices of each prostate.

Patient#	Apex			Mid				Base		
	Slice 1	Slice 2	Slice 3	Slice 4	Slice 5	Slice 6	Slice 7	Slice 8	Slice 9	Slice 10
1	35.4	84.0	91.9	93.5	94.8	95.8	95.1	92.6	86.7	67.5
2	0	72.5	85.3	89.7	92.8	94.3	93.5	90.7	84.3	54.0
3	45.5	86.2	88.5	89.4	88.8	87.2	87.5	85.6	79.9	58.9
4	76.5	88.7	89.9	90.7	91.7	93.1	92.6	88.7	77.0	50.9
5	31.6	90.1	93.6	94.3	93.9	92.5	87.6	79.3	68.5	45.3
6	20.6	84.5	92.3	96.0	96.3	96.3	94.1	89.5	83.2	69.3
7	72.4	90.9	86.6	89.1	90.7	91.3	91.1	88.1	82.3	55.6
8	60.3	86.5	92.4	93.9	92.0	87.7	84.0	81.5	77.4	67.3
9	51.8	93.4	96.1	96.0	95.2	94.4	94.3	87.8	81.2	62.8
10	25.9	67.6	84.9	87.9	89.7	91.7	89.8	87.8	81.2	62.8
11	0	54.0	68.5	79.8	88.0	84.2	79.7	76.4	70.4	50.5
12	56.0	86.5	90.7	92.8	92.7	93.3	95.3	94.8	90.9	74.6
13	84.0	90.2	91.1	94.2	95.6	95.2	92.5	91.2	90.5	61.0
14	73.1	83.9	88.9	93.5	95.6	96.4	96.0	95.4	93.0	80.0
15	52.6	75.2	85.1	87.6	88.1	87.6	87.2	84.7	75.2	53.6
16	1.5	83.6	92.2	92.0	93.3	95.6	93.4	92.0	84.7	57.5
17	0	74.0	83.4	93.4	96.3	96.0	96.0	96.0	96.0	71.4
18	43.1	86.9	90.7	94.2	95.3	94.9	94.8	93.0	88.8	59.7
19	0	54.8	84.4	90.8	94.4	94.5	90.9	91.1	88.6	71.9
20	30.0	72.5	74.2	81.3	90.2	91.8	89.6	88.5	86.0	70.7
All	38.0 ± 28.1	79.8 ± 11.1	87.5 ± 6.6	91.0 ± 4.4	92.8 ± 2.7	92.7 ± 3.5	91.2 ± 4.32	89.0 ± 5.3	83.3 ± 7.2	61.6 ± 9.6

mm for MAD and 6.90 ± 2.07 mm for MAXD. The results of slice-by-slice DSC are shown in Table 2.4, which indicate that they are consistent with the volumetric DSC results. In addition, our method delivers similar consistent results of MAD and MAXD to the DSC (see Table 2.3).

Table 2.5: Peripheral zone (PZ), central gland (CG) and whole gland (WG) mean TRE results for non rigid MR-TRUS registration.

	PZ	CG	WG
Initial alignment (mm)	2.81 ± 1.01	2.17 ± 0.60	2.44 ± 0.85
TRE (mm)	1.97 ± 0.86	1.58 ± 0.82	1.74 ± 0.84

2.3.2   Reproducibility

The variability in non-rigid registration due to manual initialization was determined by calculating the mean and standard deviations of the calculated TRE values from repeated segmentations. Manual rigid initialization variability for non-rigid registration resulted in a mean value of 1.86 mm and a standard deviation of 0.73 mm for the TREs. We performed a Mann Whitney U test on the two TRE data sets calculated for the deformable registration (20 prostates) and the reproducibility (10 prostates), which indicated no statistically significant difference between the two groups ($p > 0.05$).

2.3.3   Computation Time

The mean registration time of our method per patient was 90 ± 5 s in addition to 30 ± 5 s for initialization.

2.4   Discussion and Conclusion

This chapter describes a convex optimization approach we proposed to non-rigid image-based MR-TRUS registration, which yielded PZ, CG and WG mean TRE values of 1.97 mm, 1.90 mm, and 1.93 mm respectively, which is less than 2.5 mm [23] [38], half of the

smallest clinically significant tumor radius. The slighter higher PZ TRE value is due to deformation caused by the US probe.

Table 2.3 shows that the proposed method generated a favorable DSC value of $92.0 \pm 3.4\%$ for the mid-gland, $80.8 \pm 7.8\%$ for the apex, and $81.7 \pm 6.4\%$ for the base. The lower DSC values for the apex and base compared to the mid-gland were caused by the low degree of structure recognition in these regions for MR and especially TRUS images.

The MR-3D TRUS registration is not time critical in our approach to 3D TRUS/MR guided biopsy because the registration is performed before the intervention. The T2w-MRI and 3D TRUS images were acquired about 7 to 10 days before the intervention and suspicious lesions are delineated using the MRI information and mapped onto the TRUS image via the proposed method. Preoperative TRUS imaging permits adequate time to ensure proper multimodal alignment without prolonging the patient's biopsy procedure or level of discomfort [22]. To further shorten the computation time of registration, future work will involve optimizing the convex optimization code and implementing it in C++.

To reduce the false negative rate for prostate biopsy, we developed an alternate approach using 3D TRUS images registered with MR images with targets identified to guide the biopsy. An efficient convex optimization-based approach was proposed to extract the non-rigid MR-TRUS deformation field by registering the given two MIND descriptors, which does not require segmentation of the prostate boundaries. We applied this method on 20 patient images. The results demonstrate that the proposed method yields clinically sufficient accuracy with fewer user interactions.

Chapter 3

Non-Rigid Surface-Based MR-TRUS Registration

3.1 Introduction

The accuracy of targeting of the suspicious lesion, which has been identified in the MR image, depends on the accurate registration of the 3D TRUS and MR images. However, the prostate of the same patient may undergo deformations between the TRUS and MR imaging procedures as the altered position of the patient during the TRUS and MRI procedures, bladder filling, rectal wall motion and/or the transducer probe pressure may shift and/or deform the prostate. In order to compensate for these deformations, non-rigid registration methods are required for accurate prostate multimodal registration. Efficient and accurate non-rigid 3D MR-TRUS registration is a challenging task due to the totally different image appearances between these two image modalities, and the low degree of structure recognition in the prostate apex and base in the MR image and

44

especially TRUS images that may mislead image-based methods in those zones [40]. Therefore, a prostate surface-based registration method may help to resolve this issue by constraining the impact of artifacts and poor recognition of prostate boundaries in the MR and TRUS images. Thus, accurate manual or semi-automated prostate segmentation is required with the opportunity to edit the boundaries allowing an expert user to resolve any issues related to the different appearance of the prostate boundaries in the two image modalities.

Hu *et al.* [58] used a patient-specific finite element-based statistical motion model trained by biomechanical simulations and registered the model to 3D TRUS images, which was done by maximizing the likelihood of a particular model shape given a voxel intensity-based feature that provided an estimate of surface normal vectors at the boundary of the gland. The median TRE for 8 patients from 100 experiments was 2.40 mm. However, the method is based on the manual segmentation of the prostate gland itself, the central and peripheral zones, the pelvic bone, the rectum and the bladder on the MR images, which is time consuming.

Mitra *et al.* [59] proposed a 2D thin-plate spline-based non-linear regularization approach to align the sampled points of the segmented prostate contours, which essentially match the Bhattacharyya distance of the applied statistical shape contexts. The results showed an average TRE of 1.60 ± 1.17 mm from 20 pairs mid-gland TRUS and MR. However, the proposed framework only worked in 2D, which limits its application for clinical practice.

Singh *et al.* [60] described a manual visual method for registering MR and TRUS images, which required many user interactions to find corresponding control points ac-

cording to the anatomical features in the MR and TRUS images.

Recent work by Cool *et al.* [22] suggested a pre-biopsy MR-TRUS registration, where a landmark-based initialization with thin-plate spline (TPS) [61] yielded a mean TRE of 4.3 ± 1.2 mm, and an iterative closest point rigid initialization followed by TPS yielded a value of 5.2 ± 1.5mm. This could indicate an inaccurate gland distortion caused by a poor point correspondence between the two surfaces for TPS deformation or a mismatching of the two surfaces, which does not consider the deformation of the prostate internal architecture.

In this chapter, we developed a non-rigid prostate registration of 3D TRUS to T2-weighted MR images based on specific prostate boundary point correspondences followed by a 3D TPS deformation [61]. The primary contributions of this chapter are summarized as follows:

1) 2D slice correspondences are determined by rotationally re-slicing two segmented prostate surfaces from both 3D MR and TRUS images around a specified rotational axis, which is started by initializing 3 pairs of corresponding anatomical landmarks, and 2) a method for finding the point correspondences based on the resliced 2D corresponding slices. This approach takes into account the correspondences on the prostate surface, inside the prostate, as well as the centroid of the prostate.

3.2   Methods and Experiments

To compensate for prostate deformation, a non-rigid surface-based registration method based on Thin Plate Spline (TPS) [34] was performed. The proposed method is divided

into the following steps.

3.2.1 Initialization

We first perform a manual initialization to roughly align the prostate in the MR and TRUS images, since the prostate location and direction in the TRUS image is often arbitrary. Since with this step it is difficult to achieve robust results using an automated rigid registration method, we perform this initialization step manually. The registration to generate a rigid transform as initial alignment of the MR to 3D TRUS images makes use of 6 manually identified corresponding landmarks, which are: the end point of the peripheral zone at the apex, leftmost, rightmost, top-most, bottom-most points on the largest view of the axial slices, and the urethra at its entrance into the prostate on the MR (source) and 3D TRUS (target) images. Figure 3.1 shows an example of 6 pairs of manually placed landmarks. These corresponding landmarks are selected based on the prostate structure and architecture that can be observed on both MR and 3D TRUS images, such as the prostate boundary and/or the boundary of the bladder. The MR image is then re-sampled and resized to the same voxel size $(0.19 \times 0.19 \times 0.19 \text{ mm}^3)$ and dimensions $(448 \times 448 \times 350)$ as the TRUS image.

3.2.2 Prostate Segmentation

Following the initialization, we manually segmented the prostate surfaces from both MR and 3D TRUS images under the supervision of an experienced radiologist (C.R.). Although a number of algorithms for automated or semi-automated prostate segmentation

can be used [62] [63] [64], we choose to use manual segmentations for this study to minimize the registration error caused by the segmentation procedure. This approach allows us to study the impact of the non-rigid registration method on the accuracy and variability of the registration.

3.2.3   2D Slice Correspondences

Each pair of the 3D MR and TRUS images are automatically resliced around a rotational axis, starting from a selected corresponding view. The rotational axis is specified using 2 of the manually identified anatomical landmarks (See Figure 3.2): the end point of the peripheral zone at the apex and the urethra at its entrance into the prostate. The landmarks for generating the first corresponding view uses the 2 points for setting the rotational axis, as well as the bottom-most point on the largest view of the axial slices.

2D slice correspondences are determined by rotationally reslicing the two manually segmented prostate surfaces from the 3D MR and TRUS images around the specified rotational axis. Figure 3.3 shows an example of the resliced 2D contours.

The point correspondences are found based on the boundaries of the 2D slice correspondences instead of finding the 3D point correspondences directly, because once the first corresponding slice is manually confirmed, the correspondences are established for each resliced contour, and there is little non-rigid deformation between resliced-planes.

3.2.4 Point Correspondences

From the resliced corresponding 2D contours, the point correspondences is then achieved by automatically selecting 8 points for each contour on an equal contour distance basis (See Figure 3.4). This procedure assumes the prostate perimeter is conserved between the 3D TRUS and MR images. While this is not true for arbitrary shapes, because the deformation of the prostate is not large, this approach may be useful. The starting point for each contour is the corresponding landmark of the urethra at its entrance into the prostate. We also take into account the centroid point of the prostate, as well as the mid-points between the centroid and the points already found on each contour to be the corresponding points for the registration.

Based on the point correspondences, we apply a 3D TPS [34] on the 3D point cloud (i.e., the corresponding points) in the MR image in order to align them to the corresponding points of the target 3D TRUS image. TPS interpolates specified points while minimizing an approximate curvature (integrated squared second derivative), resulting in a smooth deformation without unexpected ripples and variations.

The set of points in MR images are denoted as p_i, and in the TRUS, the corresponding points are q_i, where $i = 1, ... N$, N represents the number of points in each image, and the transformation that maps two images by u. The registration function $J_\lambda(u)$ consists of a landmark registration metric term and a TPS term $J_m^d(u)$ that regularizes the transformation:

$$J_\lambda(u) = \frac{1}{N} \sum_{i=1}^{N} [q_i - u(p_i)]^T S_n^{-1} [q_i - u(p_i)] + \lambda J_m^d(u) , \qquad (3.1)$$

In equation 3.1, the covariance matrix S_n is a 3×3 matrix and represents anisotropic landmark localization errors, d refers to the dimension of the image and m to the chosen derivative order of the functional. The term $J_m^d(u)$ defines the TPS and controls the smoothness of the transformation. The minimization of equation 3.1 results in a smooth transformation that approximated the distance between the landmark sets, the λ parameter controls the weighting between the two terms, and the transformation becomes smoother as λ increases.

3.2.5   Experiments

This study was conducted with images acquired with the approval of our institutions Human Subjects Research Ethics Board and with the informed consent of all subjects. The proposed surface-based approach to non-rigid MR-3D TRUS registration was implemented partially using Matlab R2011b (version 7.13.0.564; Natick, MA, USA) and partially C++. The experiments were conducted on a Windows desktop with an Intel i7-3770 CPU (3.4 GHz). The mean computation time was determined by calculating the mean of execution time for running the program with 10 patients 3D TRUS and MR image pairs.

Materials

The T2-weighted MR images and the corresponding 3D TRUS images were acquired of 17 patients scheduled prostate biopsy. The MR images were acquired using a body coil with a whole-body 3T Excite 12.0 MRI system (GEHC, Milwaukee, WI, USA) with an image size of $512 \times 512 \times 36$ voxels with a voxel size of $0.27 \times 0.27 \times 2.2$ mm^3. The 3D
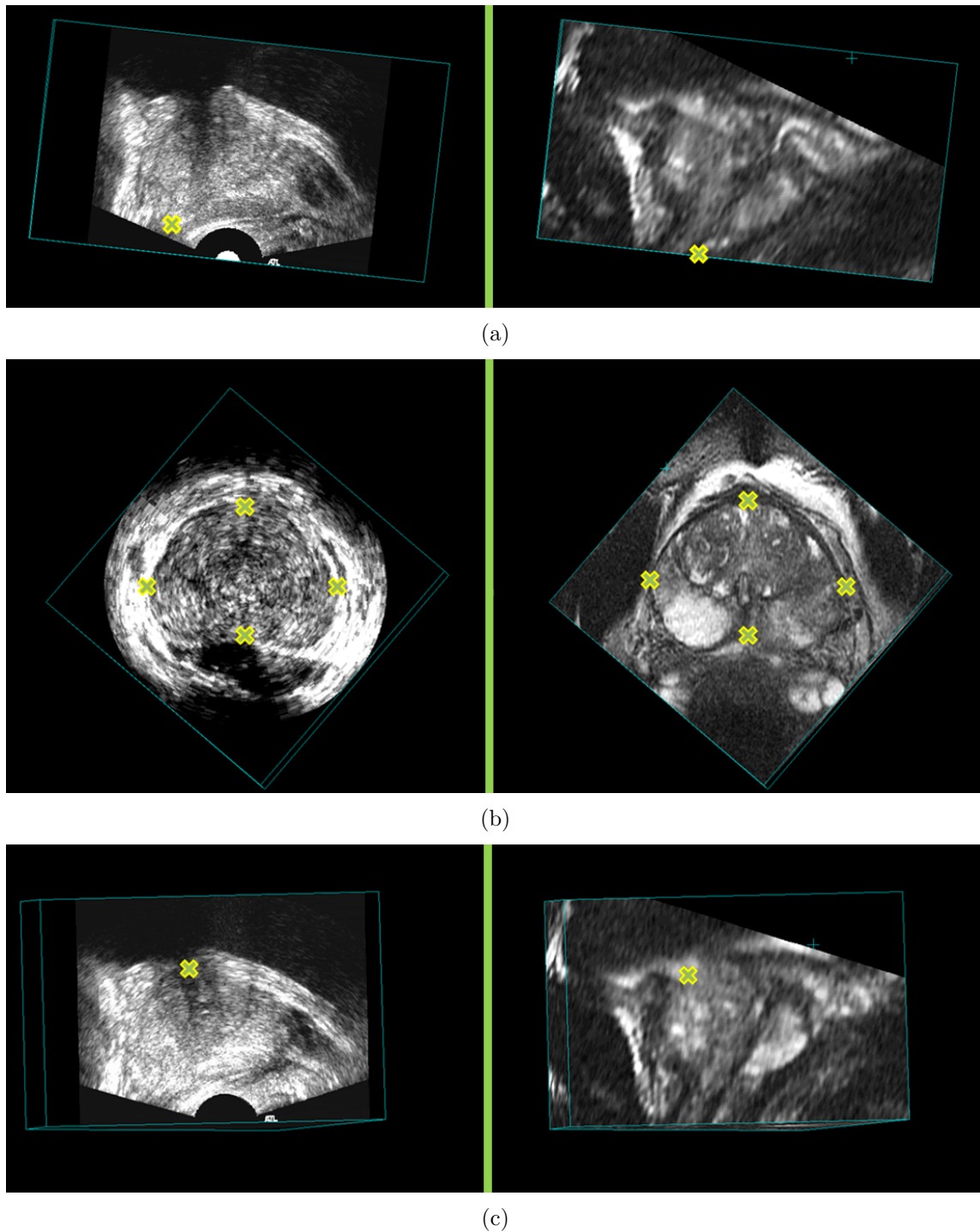
Figure 3.1: Yellow crosses indicate anatomical landmarks in the 3D TRUS (left column) and corresponding MR images (right column), (a) shows the end points of peripheral zone at the apex, (b) shows the corresponding points with the largest view of the axial slices, and (c) shows the corresponding entrance points of urethra into the prostate.

(a)

(b)
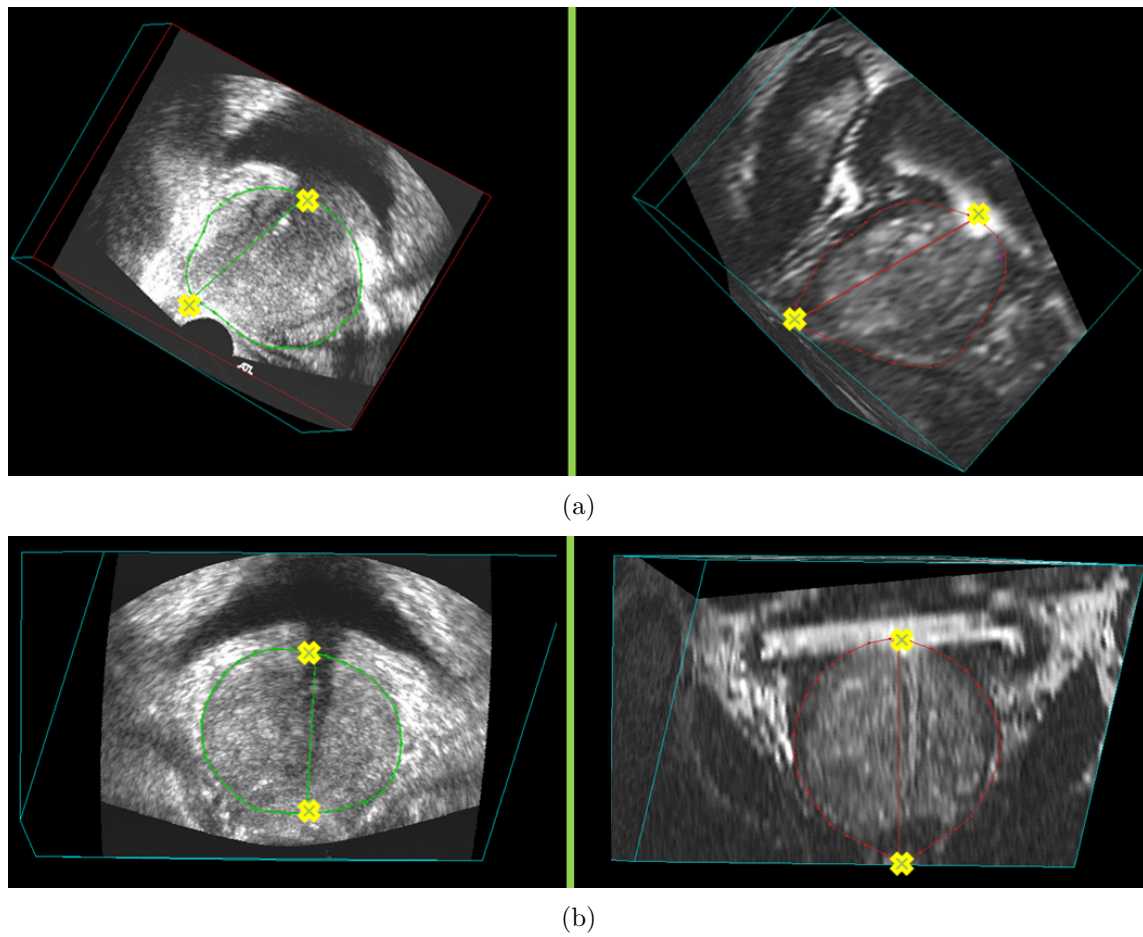
Figure 3.2: Rotational axis based on the corresponding anatomical landmarks (yellow crosses) in the 3D TRUS (left column) and corresponding MR images (right column). (a) from sagittal view, and (b) from coronal view.
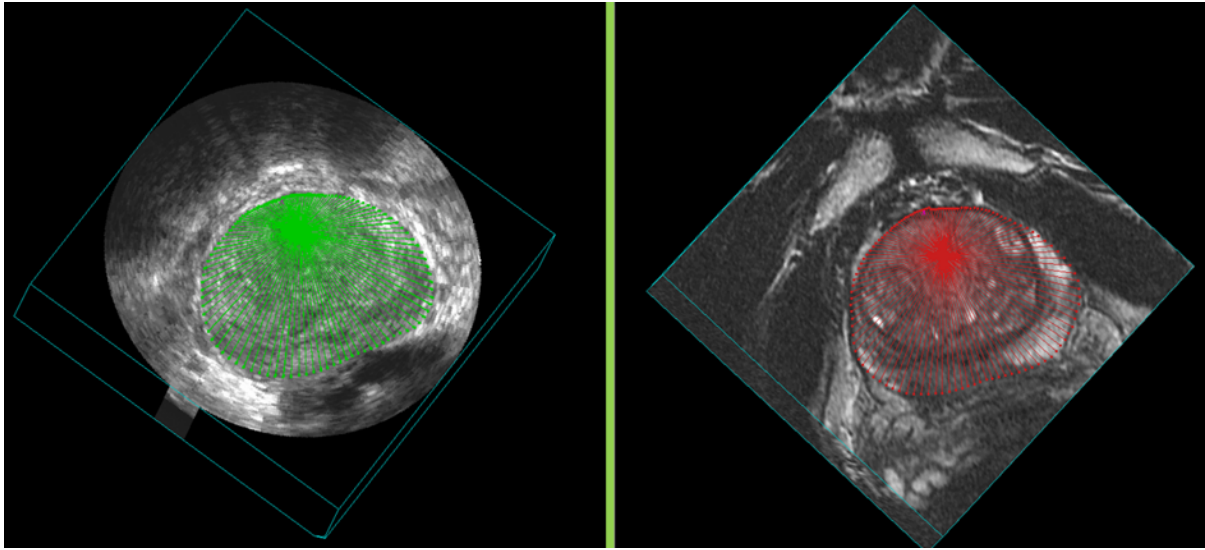
Figure 3.3: Example of resliced corresponding 2D contours from axial view in the 3D TRUS (left column) and corresponding MR images (right column)
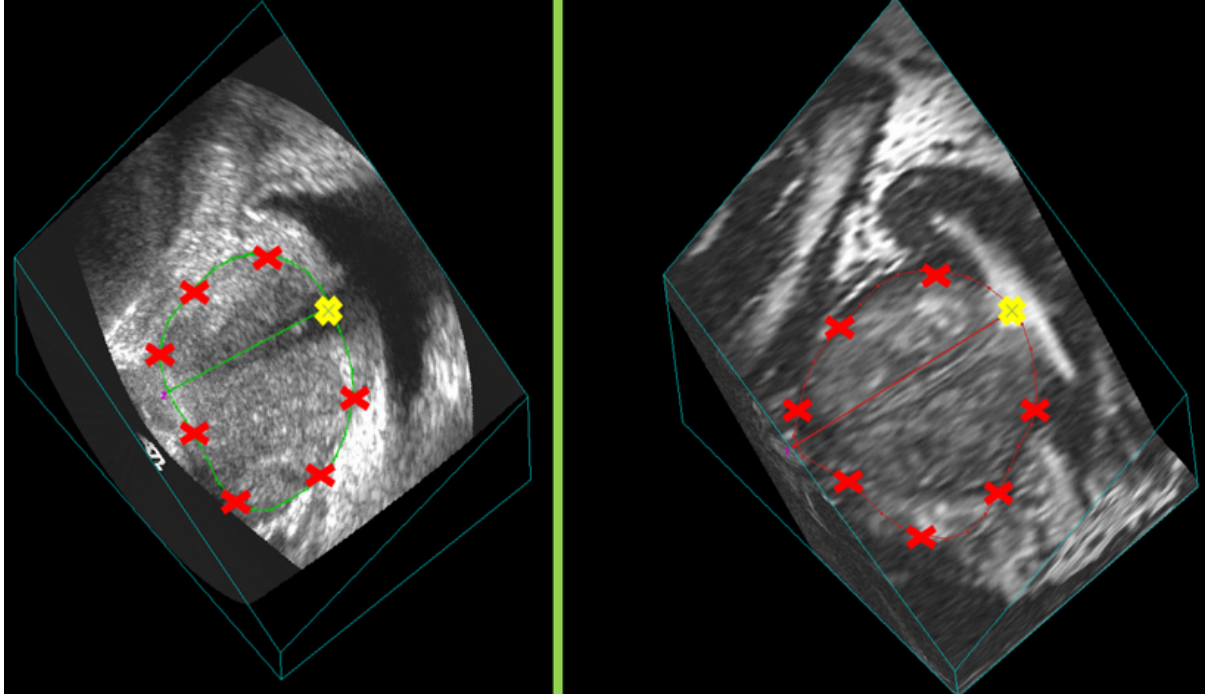
Figure 3.4: A sample of point correspondence on a pair of corresponding 2D contours in the 3D TRUS (left column) and corresponding MR images (right column).

TRUS images were acquired using a 3D TRUS mechanical scanning system developed in our laboratory [18], using a Philips HDI-5000 US machine with a Philips end-firing C9-5 transducer (Philips, Bothell, WA, USA). The 3D TRUS image size was $448 \times 448 \times 350$ voxels with a voxel size of $0.19 \times 0.19 \times 0.19$ mm^3.

3.2.6   Evaluation

Accuracy

We measured the target registration error (TRE) [36] [37] as an indication of the overall misalignment of manually identified corresponding intrinsic fiducials in the MR and 3D TRUS images. The approximate corresponding landmarks used for rigid initialization were not used in the evaluation. Eighty-six fiducials (calcifications and cysts) were manually identified in the 17 image pairs by a trained operator (Y.S.) under the supervision of an experienced radiologist (C.R.). Of the 86 fiducials selected, 41 were within the peripheral zone (PZ), known to be the most common site harboring cancer [55] and subject to deformation caused by the US transducer during biopsy. Accurate biopsy targeting relies on corrections being made for this deformation. We also measured the fiducial localization error (FLE) [37] to allow determination whether fiducial identification dominated the TRE. For FLE determination, the trained operator identified 30 fiducials in 10 prostate image pairs (three fiducials/prostate) five times over five days and recorded their coordinates once per day.

Statistical analyses were performed in SPSS Version 15.0 (SPSS, Chicago, IL) to determine if there was a statistical significant difference in the TREs between the manual

rigid registration and surface-based non-rigid registration.

Reproducibility

The variability of our registration method was determined by calculating the dependence of the non-rigid registration on the manually selecting 3 corresponding fiducials for finding the first corresponding slice (two of the three are using to specify the rotational axis). To study the effects of variability of selecting the 3 fiducials during initialization on TRE, 5 patients 3D prostate MR-TRUS image pairs were selected. These 3D MR-TRUS images were initialized using manually identified fiducials selected by two trained operators, five times each. Each initialization procedure was performed at least one day after the previous session in order to minimize learning eects. The initialized MR-TRUS images were then used for surface-based non-rigid registration. TRE values for each trial and the overall TRE for all patients were then calculated.

3.3   Results

The median and root mean square (RMS) TRE results for the initial rigid alignment and the non-rigid registration are summarized in Table 3.1, which shows an overall mean TRE of 3.50 ± 1.34 mm for the rigid registration and 2.24 ± 0.71 mm for the non-rigid registration.

We performed a Shapiro-Wilk test on the TREs calculated for the initial rigid registration and surface-based non-rigid registration data sets. This test revealed the TRE distributions of rigid transform and non-rigid registration were both non-normal ($p < 0.05$).

Table 3.1: TREs for 17 patient image pairs.

Patient#	Rigid RMS TRE (mm)		Non-rigid RMS TRE (mm)	
	Median	Mean ± std	Median	Mean ±std
1	2.95	2.97 ± 0.31	2.53	2.55 ± 0.52
2	4.83	4.88 ± 0.09	3.73	3.37 ± 0.77
3	2.80	2.73 ± 0.16	2.32	2.33 ± 0.06
4	2.50	2.53 ± 0.21	2.69	2.64 ± 0.58
5	1.78	1.98 ± 0.47	2.46	2.29 ± 0.48
6	2.66	3.08 ± 0.89	2.43	2.62 ± 1.02
7	4.67	4.70 ± 0.68	1.69	1.70 ± 0.05
8	1.78	1.86 ± 0.30	1.67	1.58 ± 0.29
9	1.46	1.47 ± 0.21	1.35	1.30 ± 0.30
10	4.16	4.16 ± 0.14	1.52	1.52 ± 0.07
11	3.37	3.51 ± 0.81	1.82	1.74 ± 0.34
12	2.10	2.16 ± 0.38	1.61	1.64 ± 0.12
13	3.41	3.31 ± 1.23	1.72	2.56 ± 1.20
14	5.66	5.53 ± 0.59	2.31	2.34 ± 0.57
15	2.31	2.37 ± 0.73	2.20	2.21 ± 0.32
16	2.62	2.58 ± 0.15	1.68	2.12 ± 0.74
17	4.73	4.46 ± 1.02	3.36	3.26 ± 0.67
All	2.80	3.50 ± 1.34	1.96	2.24 ± 0.71

Table 3.2: TREs for PZ, CG and WG.

	PZ	CG	WG
# of fiducials	41	45	86
Mean (mm)	2.08 ± 0.65	2.37 ± 0.75	2.24 ± 0.71
Median (mm)	1.77	2.30	1.96

Thus, we performed a Wilcoxon Sign Rank test for non-normal distributions, which indicated a significant difference between the TRE values of the two study groups, ($p < 0.01$).

The FLE was 0.21 mm for 3D TRUS images, and 0.18 mm for MR. Thus, the FLEs did not dominate the overall TRE. The mean and median TRE values for the PZ, central gland (CG) and whole gland (WG) are summarized in 3.2, which shows that the mean TRE for the CG is about 0.13 mm larger than the value for the PZ. Figure 5(a) shows the frequency distribution of all measured TREs of the initial rigid alignment and Figure 5(b) the surface-based non-rigid registration for the WG and PZ. Figure 5(b) shows that 75.6% of the TRE values for WG and 80.5% for PZ are smaller than 2.5 mm. Figure 3.5(a) shows the frequency distribution of all measured TREs of the initial rigid alignment and Figure 3.5(b) the surface-based non-rigid registration for the WG and PZ. Figure 3.5(b) shows that 75.6% of the TRE values for WG and 80.5% for PZ are smaller than 2.5 mm.

Reproducibility

The variability in surface-based non-rigid registration due to manually selecting the rotational axis was determined by calculating the mean and standard deviations of the calculated TRE values from repeated axis selections. The variability of manual rotational axis selection for non-rigid registration resulted in a mean TRE value of 2.38 mm and a standard deviation of 0.99 mm. We performed a Mann Whitney U test on the two
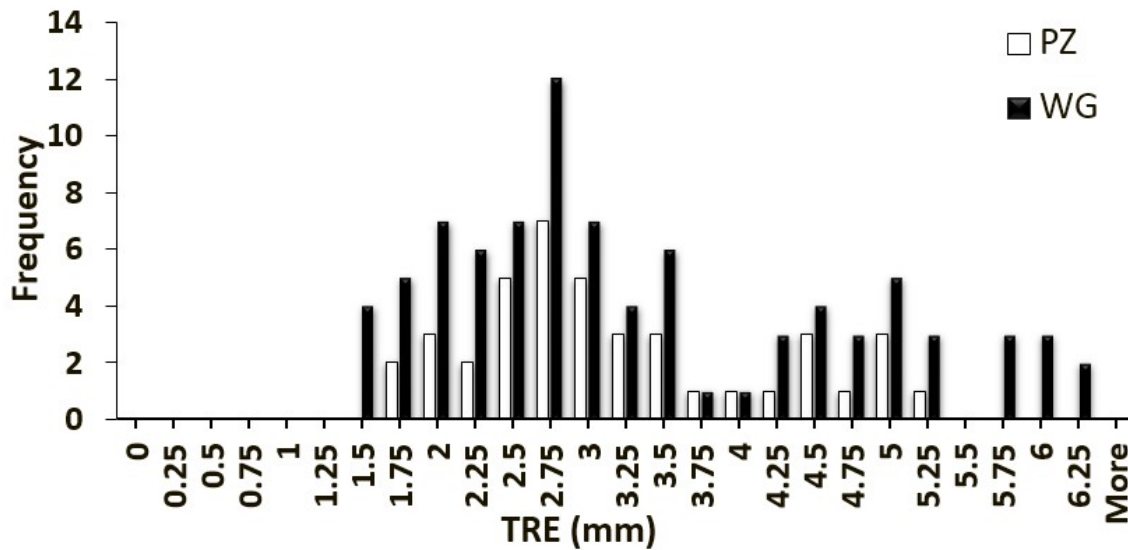
(a)
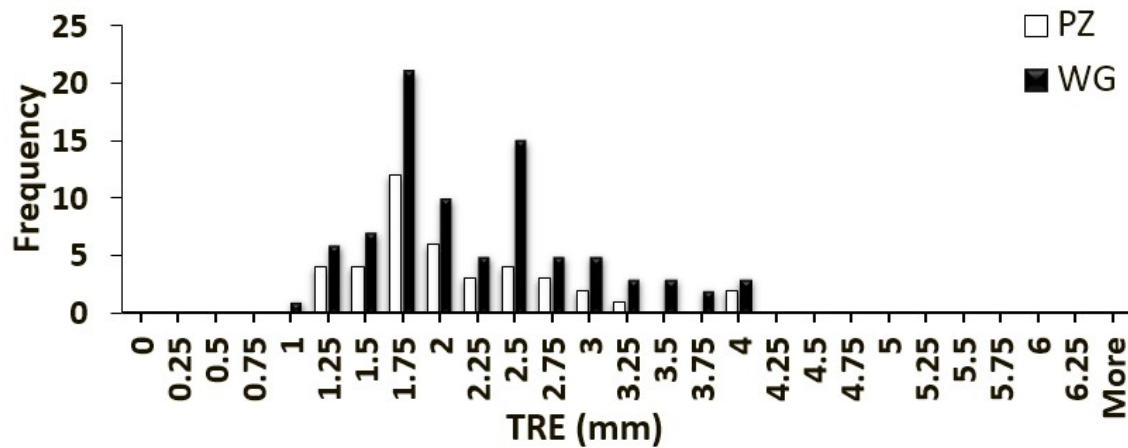
(b)

Figure 3.5: WG (black) and PZ (white) frequency distributions of: (a) rigid alignment TRE between all 86 fiducial pairs, and (b) surface-based non-rigid registration TRE.

TRE data sets calculated for the deformable registration (17 prostates) and the reproducibility (5 prostates), which indicated no significant statistical difference between the two groups ($p > 0.05$).

Computation Time

The mean registration time of our method per patient was 60 ± 5 s in addition to 4 ± 1 minutes for manually segmenting one patients MR and TRUS images, and 60 ± 5 s for manually selecting the rotational axis.

3.4 Discussion and Conclusion

In this work, we proposed an approach to find point correspondences for surface-based non-rigid 3D MR-TRUS registration, which yielded PZ, CG and WG mean TRE values of 2.08 mm, 2.37 mm, and 2.24 mm respectively, which is less than 2.5 mm, half of the smallest clinically significant tumor radius [23] [38]. Although the PZ is deformed by pressure of the TRUS transducer, the PZ TRE is slighter lower than the CG, because the surface-based registration compensates better the deformation as this region is closer to the prostate boundary.

To reduce the false negative rate of conventional 2D TRUS guided biopsy prostate biopsy, we developed a 3D TRUS-guided biopsy system, which makes use of TRUS images registered with MR images with identified tumor targets to guide the biopsy. We proposed an efficient surface-based approach employing: 1) rotationally resliced two corresponding segmented prostate surfaces from both 3D MR and TRUS images around

a specified axis, and 2) a novel approach to find point correspondences, which takes into account the correspondences on the prostate surface, inside the prostate, as well as the centroid of the prostate. We applied this method on 17 patient images and our results demonstrate that the proposed method yields clinically sufficient accuracy.

Chapter 4

Summary

To reduce the false negative rate for image-guided prostate biopsy, this thesis summarizes two 3D MR-TRUS image registration methods. The registration procedure is critical for targeting the suspicious lesions identified in the MR image. Accurate registration allows for improved planning, targeting and needle guidance.

The method described in Chapter 2 makes use of a convex optimization approach to extract the non-rigid MR-TRUS deformation field by registering the given two MIND descriptors, which do not require segmentation of the prostate boundaries. We applied this method on 20 patient images, which yielded prostate PZ, CG and WG mean TRE values of 1.97 mm, 1.90 mm, and 1.93 mm respectively, which is less than 2.5 mm, half of the smallest clinically significant tumor radius [23] [38]. The higher PZ TRE value might be due to deformation caused by the US probe. This method also generated a favorable DSC value of $92.0 \pm 3.4\%$ for the mid-gland, $80.8 \pm 7.8\%$ for the apex, and $81.7 \pm 6.4\%$ for the base. The lower DSC values for the apex and base compared to the mid-gland might be caused by the low degree of structure recognition in these regions for MR and

especially TRUS images.

Our mean TRE of 1.93 ± 0.73 mm is higher than the value of 1.60 ± 1.17 mm in Mitra *et al.* [59]. However, their method needed a segmented prostate surface for both MR and TRUS images, and the established MR-TRUS slice correspondence, which is difficult to achieve in practice. Our RMS TRE of 1.76 mm is lower than the 2.4 mm achieved by Hu *et al.* [58]. They required additional segmentations of the MR prostate gland , pelvic bone, rectum, and bladder for biomechanical modeling (approximately 45 min per patient).

The T2-weighted MR and 3D TRUS images were acquired about 7 to 10 days before the intervention and suspicious lesions are delineated using the MR information and mapped onto the TRUS image via the proposed method. Preoperative TRUS imaging permits adequate time to ensure proper multimodal alignment without prolonging the patient's biopsy procedure or level of discomfort [22]. The mean registration time of this method per patient is 90 ± 5 s in addition to 30 ± 5 s for initialization. To further shorten the computation time of registration, future work will involve optimizing the convex optimization code and implementing it in C++.

Chapter 3 describes an surface-based non-rigid 3D MR-TRUS registration approach employing:

1) rotationally resliced two corresponding segmented prostate surfaces from both 3D MR and TRUS images around a specified axis, and

2) a novel approach to find point correspondences, which takes into account the correspondences on the prostate surface, inside the prostate, as well as the centroid of the prostate.

We applied this method on 17 patient images and our results demonstrate that the proposed method yields clinically sufficient accuracy. The mean TRE values for PZ, CG and WG showed 2.08 mm, 2.37 mm, and 2.24 mm respectively, which is also less than 2.5 mm. Although the PZ is deformed by pressure of the TRUS transducer, the PZ TRE is slighter lower than the CG, because the surface-based registration compensates better the deformation as this region is closer to the prostate boundary.

The main time consuming part of the whole registration pipeline is the manual segmentation for each patients 3D MR and TRUS image. We are currently exploring alternative, automatic methods for segmenting the prostate, which would significantly reduce the segmentation time [62] [63] [64]. Implementing the code in C++ will shorten the computation time of registration, particularly for achieving point correspondences.

Comparing the performance of the image-based to the surface-based method, the mean TRE value from image-based registration for WG is 0.31 mm lower than the surface-based result, whereas the registration's computation time is 30 s longer (calculation based on the non-optimized codes). In terms of the consideration for clinical use, the surface-based method is recommended, because it's less affected by the image artifact. Thereby, it could be used for every case.

Bibliography

[1] Canadian Cancer Society [Online], "http://www.cancer.ca," 2012.

[2] Cancer Research UK [Online], "http://www.cancerresearchuk.org," 2013.

[3] National Cancer Institute [Online], "http://www.cancer.gov," 2012.

[4] Y. Sun, J. Yuan, W. Qiu, M. Rajchl, C. Romagnoli, and A. Fenster, "Three-dimensional non-rigid MR-TRUS registration using dual optimization," *Submitted to IEEE Transactions on Image Processing*, 2013.

[5] L. Shi, W. Liu, H. Zhang, Y. Xie, and D. Wang, "A survey of GPU-based medical image computing techniques," *Quantitative imaging in medicine and surgery*, vol. 2, no. 3, p. 188, 2012.

[6] M. Rifkin, *Ultrasound of the prostate: imaging in the diagnosis and therapy of prostatic disease.* Lippincott-Raven Publishers, 1997.

[7] M. Norberg, L. Egevad, L. Holmberg, P. Sparén, B. Norlén, and C. Busch, "The sextant protocol for ultrasound-guided core biopsies of the prostate underestimates the presence of cancer," *Urology*, vol. 50, no. 4, pp. 562 – 566, 1997.

[8] K. L. Zakian, K. Sircar, H. Hricak, H. N. Chen, A. Shukla-Dave, S. Eberhardt, M. Muruganandham, L. Ebora, M. W. Kattan, V. E. Reuter, P. T. Scardino, and J. A. Koutcher, "Correlation of proton MR spectroscopic imaging with gleason score based on step-section pathologic analysis after radical prostatectomy," *Radiology*, vol. 234, no. 3, pp. 804–814, 2005.

[9] N. B. Delongchamps, M. Rouanne, T. Flam, F. Beuvon, M. Liberatore, M. Zerbib, and F. Cornud, "Multiparametric magnetic resonance imaging for the detection and localization of prostate cancer: combination of T2-weighted, dynamic contrast-enhanced and diffusion-weighted imaging," *BJU international*, vol. 107, no. 9, pp. 1411–1418, 2011.

[10] K. Kitajima, Y. Kaji, Y. Fukabori, K.-i. Yoshida, N. Suganuma, and K. Sugimura, "Prostate cancer detection with 3T MRI: Comparison of diffusion-weighted imaging and dynamic contrast-enhanced MRI in combination with T2-weighted imaging," *Journal of Magnetic Resonance Imaging*, vol. 31, no. 3, pp. 625–631, 2010.

[11] G. A. Sonn, S. Natarajan, D. J. Margolis, M. MacAiran, P. Lieu, J. Huang, F. J. Dorey, and L. S. Marks, "Targeted biopsy in the detection of prostate cancer using an office based magnetic resonance ultrasound fusion device," *The Journal of Urology*, vol. 189, no. 1, pp. 86 – 92, 2013.

[12] S. H. Lee, K. K. Park, K. H. Choi, B. J. Lim, J. H. Kim, S. W. Lee, and B. H. Chung, "Is endorectal coil necessary for the staging of clinically localized prostate cancer?

comparison of non-endorectal versus endorectal MR imaging," *World journal of urology*, vol. 28, no. 6, pp. 667–672, 2010.

[13] I. W. van der CRUIJSEN-KOETER, A. N. Vis, M. J. Roobol, M. F. Wildhagen, H. J. de KONING, T. van der KWAST, and F. H. SCHRÖDER, "Comparison of screen detected and clinically diagnosed prostate cancer in the European randomized study of screening for prostate cancer, section rotterdam," *The Journal of urology*, vol. 174, no. 1, pp. 121–125, 2005.

[14] American Cancer Society [Online], "American Cancer Society: Prostate cancer: early detection," 2013.

[15] F. H. Schröder, H. B. Carter, T. Wolters, R. C. van den Bergh, C. Gosselaar, C. H. Bangma, and M. J. Roobol, "Early detection of prostate cancer in 2007: part 1: PSA and PSA kinetics," *European urology*, vol. 53, no. 3, pp. 468–477, 2008.

[16] P. Emiliozzi, P. Scarpone, F. DePAULA, M. Pizzo, G. Federico, A. Pansadoro, M. Martini, and V. Pansadoro, "The incidence of prostate cancer in men with prostate specific antigen greater than 4.0 ng/ml:: A randomized study of 6 versus 12 core transperineal prostate biopsy," *The Journal of urology*, vol. 171, no. 1, pp. 197–199, 2004.

[17] D. W. Cool, M. J. Connolly, S. Sherebrin, R. Eagleson, J. I. Izawa, J. Amann, C. Romagnoli, W. M. Romano, and A. Fenster, "Repeat prostate biopsy accuracy: Simulator-based comparison of two-and three-dimensional transrectal US modalities1," *Radiology*, vol. 254, no. 2, pp. 587–594, 2010.

[18] J. Bax, D. Cool, L. Gardi, K. Knight, D. Smith, J. Montreuil, S. Sherebrin, C. Romagnoli, and A. Fenster, "Mechanically assisted 3D ultrasound guided prostate biopsy system.," *Med. Phys.*, vol. 35, no. 12, pp. 5397–5410, 2008.

[19] A. K. Singh, J. Kruecker, S. Xu, N. Glossop, P. Guion, K. Ullman, P. L. Choyke, and B. J. Wood, "Initial clinical experience with real-time transrectal ultrasonography-magnetic resonance imaging fusion-guided prostate biopsy," *BJU international*, vol. 101, no. 7, pp. 841–845, 2007.

[20] J. A. Long, V. Daanen, A. Moreau-Gaudry, J. Troccaz, J.-J. Rambeaud, and J.-L. Descotes, "Prostate biopsies guided by three-dimensional real-time (4-D) transrectal ultrasonography on a phantom: comparative study versus two-dimensional transrectal ultrasound-guided biopsies," *European urology*, vol. 52, no. 4, pp. 1097–1105, 2007.

[21] F. Shen, K. Shinohara, D. Kumar, A. Khemka, A. R. Simoneau, P. N. Werahera, L. Li, Y. Guo, R. Narayanan, L. Wei, *et al.*, "Three-dimensional sonography with needle tracking role in diagnosis and treatment of prostate cancer," *Journal of Ultrasound in Medicine*, vol. 27, no. 6, pp. 895–905, 2008.

[22] D. Cool, J. Bax, C. Romagnoli, A. Ward, L. Gardi, V. Karnik, J. Izawa, J. Chin, and A. Fenster, "Fusion of MRI to 3D TRUS for mechanically-assisted targeted prostate biopsy: System design and initial clinical experience," in *Prostate Cancer Imaging. Image Analysis and Image-Guided Interventions* (A. Madabhushi, J. Dowling,

H. Huisman, and D. Barratt, eds.), vol. 6963 of *Lecture Notes in Computer Science*, pp. 121–133, Springer Berlin / Heidelberg, 2011.

[23] V. Karnik, A. Fenster, J. Bax, D. Cool, L. Gardi, I. Gyacskov, C. Romagnoli, and A. Ward, "Assessment of image registration accuracy in three-dimensional transrectal ultrasound guided prostate biopsy," *Medical physics*, vol. 37, p. 802, 2010.

[24] V. V. Karnik, A. Fenster, J. Bax, C. Romagnoli, and A. D. Ward, "Evaluation of intersession 3D-TRUS to 3D-TRUS image registration for repeat prostate biopsies," *Med. Phys.*, vol. 38, pp. 1832–1843, Apr 2011.

[25] T. D. Silva, A. Fenster, D. W. Cool, L. Gardi, C. Romagnoli, J. Samarabandu, and A. D. Ward, "2D-3D rigid registration to compensate for prostate motion during 3D TRUS-guided biopsy," *Medical Physics*, vol. 40, no. 2, p. 022904, 2013.

[26] N. Hara, M. Okuizumi, H. Koike, M. Kawaguchi, and V. Bilim, "Dynamic contrast-enhanced magnetic resonance imaging (DCE-MRI) is a useful modality for the precise detection and staging of early prostate cancer," *The Prostate*, vol. 62, no. 2, pp. 140–147, 2005.

[27] J. J. Futterer, S. Heijmink, T. W. Scheenen, J. Veltman, H. J. Huisman, P. Vos, C. de Kaa, J. A. Witjes, P. F. Krabbe, A. Heerschap, *et al.*, "Prostate cancer localization with dynamic contrast-enhanced MR imaging and proton MR spectroscopic imaging," *Radiology-Radiological Society of North America*, vol. 241, no. 2, pp. 449–458, 2006.

[28] M. A. Haider, T. H. van der Kwast, J. Tanguay, A. J. Evans, A.-T. Hashmi, G. Lockwood, and J. Trachtenberg, "Combined T2-weighted and diffusion-weighted MRI for localization of prostate cancer," *American Journal of Roentgenology*, vol. 189, no. 2, pp. 323–328, 2007.

[29] J. Scheidler, H. Hricak, D. B. Vigneron, K. K. Yu, D. L. Sokolov, L. R. Huang, C. J. Zaloudek, S. J. Nelson, P. R. Carroll, and J. Kurhanewicz, "Prostate cancer: Localization with three-dimensional proton MR spectroscopic imaging-clinicopathologic study," *Radiology*, vol. 213, no. 2, pp. 473–480, 1999.

[30] K. K. Yu, J. Scheidler, H. Hricak, D. B. Vigneron, C. J. Zaloudek, R. G. Males, S. J. Nelson, P. R. Carroll, and J. Kurhanewicz, "Prostate cancer: Prediction of extracapsular extension with endorectal MR imaging and three-dimensional proton MR spectroscopic imaging 1," *Radiology*, vol. 213, no. 2, pp. 481–488, 1999.

[31] S. Xu, J. Kruecker, B. Turkbey, N. Glossop, A. K. Singh, P. Choyke, P. Pinto, and B. J. Wood, "Real-time MRI-TRUS fusion for guidance of targeted prostate biopsies," *Computer Aided Surgery*, vol. 13, no. 5, pp. 255–264, 2008.

[32] M. Sonka and J. M. Fitzpatrick, "Handbook of medical imaging(volume 2, medical image processing and analysis)," SPIE- The international society for optical engineering, 2000.

[33] P. J. Besl and N. D. McKay, "Method for registration of 3-d shapes," in *Robotics-DL tentative*, pp. 586–606, International Society for Optics and Photonics, 1992.

[34] F. L. Bookstein, "Principal warps: Thin-plate splines and the decomposition of deformations," *IEEE Transactions on pattern analysis and machine intelligence*, vol. 11, no. 6, pp. 567–585, 1989.

[35] F. Maes, A. Collignon, D. Vandermeulen, G. Marchal, and P. Suetens, "Multimodality image registration by maximization of mutual information," *Medical Imaging, IEEE Transactions on*, vol. 16, no. 2, pp. 187–198, 1997.

[36] J. V. Hajnal, *Medical image registration*. CRC PressI Llc, 2001.

[37] J. Fitzpatrick, J. West, and J. Maurer, C.R., "Predicting error in rigid-body point-based registration," *IEEE TMI*, vol. 17, pp. 694 –702, Oct 1998.

[38] J. I. Epstein, H. Sanderson, H. B. Carter, and D. O. Scharfstein, "Utility of saturation biopsy to predict insignificant cancer at radical prostatectomy," *Urology*, vol. 66, no. 2, pp. 356–360, 2005.

[39] M. P. Heinrich, M. Jenkinson, M. Bhushan, T. Matin, F. V. Gleeson, S. M. Brady, and J. A. Schnabel, "Mind: Modality independent neighbourhood descriptor for multi-modal deformable registration," *MedIA*, vol. 16, no. 7, pp. 1423 – 1435, 2012.

[40] Y. Sun, J. Yuan, M. Rajchl, W. Qiu, C. Romagnoli, and A. Fenster, "Efficient convex optimization approach to 3D non-rigid MR-TRUS registration," in *Medical Image Computing and Computer-Assisted Intervention–MICCAI 2013*, pp. 195–202, Springer, 2013.

[41] Y. Sun, W. Qiu, C. Romagnoli, and A. Fenster, "3D non-rigid surface-based MR-TRUS registration for image-guided prostate biopsy," in *SPIE Medical Imaging*, pp. 90362J–90362J, International Society for Optics and Photonics, 2014.

[42] F. Maes, A. Collignon, D. V, G. Marchal, and P. Suetens, "Multimodality image registration by maximization of mutual information," *IEEE transactions on Medical Imaging*, vol. 16, pp. 187–198, 1997.

[43] J. Modersitzki, *Numerical Methods for Image Registration*. Numerical Mathematics and Scientific Computation, Oxford University Press, 2004.

[44] B. K. P. Horn and B. G. Schunck, "Determining optical flow," *ARTIFICAL INTEL-LIGENCE*, vol. 17, pp. 185–203, 1981.

[45] J. Weickert and C. Schnörr, "Variational optic flow computation with a spatio-temporal smoothness constraint," *J. Math. Imaging and Vision*, vol. 14, no. 3, pp. 245–255, 2001.

[46] J. Yuan, E. Bae, X.-C. Tai, and Y. Boykov, "A continuous max-flow approach to potts model," in *ECCV*, 2010.

[47] J. Yuan, E. Ukwatta, X.-C. Tai, A. Fenster, and C. Schnoerr, "A fast global optimization-based approach to evolving contours with generic shape prior," Technical report CAM-12-38, UCLA, 2012.

[48] A. Buades, B. Coll, and J.-M. Morel, "A non-local algorithm for image denoising," in *CVPR*, pp. 60–65, 2005.

[49] G. Hermosillo, C. Chefd'Hotel, and O. D. Faugeras, "Variational methods for mul-
     timodal image matching," *International Journal of Computer Vision*, vol. 50, no. 3,
     pp. 329–343, 2002.

[50] C. Wachinger and N. Navab, "Entropy and laplacian images: Structural representa-
     tions for multi-modal registration," *Medical Image Analysis*, vol. 16, no. 1, pp. 1–17,
     2012.

[51] M. Baust, D. Zikic, and N. Navab, "Diffusion-based regularisation strategies for
     variational level set segmentation," in *BMVC*, pp. 1–11, 2010.

[52] D. P. Bertsekas, *Nonlinear Programming*. Athena Scientific, September 1999.

[53] J. Yuan, E. Bae, and X. Tai, "A study on continuous max-flow and min-cut ap-
     proaches," in *CVPR*, 2010.

[54] S. S. Mahdavi, N. Chng, I. Spadinger, W. J. Morris, and S. E. Salcudean, "Semi-
     automatic segmentation for prostate interventions," *Medical Image Analysis*, vol. 15,
     no. 2, pp. 226 – 237, 2011.

[55] J. E. McNeal, E. A. Redwine, F. S. Freiha, and T. A. Stamey, "Zonal distribution
     of prostatic adenocarcinoma: correlation with histologic pattern and direction of
     spread," *The American journal of surgical pathology*, vol. 12, no. 12, pp. 897–906,
     1988.

[56] K. Zou, S. Warfield, A. Bharatha, C. Tempany, M. Kaus, S. Haker, W. Wells,
     F. Jolesz, and R. Kikinis, "Statistical validation of image segmentation quality based
     on a spatial overlap index," *Academic Radiology*, vol. 11, no. 2, pp. 178–189, 2004.

[57] W. Qiu, J. Yuan, E. Ukwatta, D. Tessier, and A. Fenster, "Rotational-slice-based prostate segmentation using level set with shape constraint for 3D end-firing TRUS guided biopsy," in *MICCAI(Part 1), LNCS 7510*, pp. 536–543, 2012.

[58] Y. Hu, H. U. Ahmed, Z. Taylor, C. Allen, M. Emberton, D. Hawkes, and D. Barratt, "MR to ultrasound registration for image-guided prostate interventions," *Medical Image Analysis*, vol. 16, no. 3, pp. 687 – 703, 2012.

[59] J. Mitra, Z. Kato, R. Marti, A. Oliver, X. Llad, D. Sidib, S. Ghose, J. C. Vilanova, J. Comet, and F. Meriaudeau, "A spline-based non-linear diffeomorphism for multimodal prostate registration.," *Medical Image Analysis*, vol. 16, no. 6, pp. 1259–1279, 2012.

[60] A. K. Singh, J. Kruecker, S. Xu, N. Glossop, P. Guion, K. Ullman, P. L. Choyke, and B. J. Wood, "Initial clinical experience with real-time transrectal ultrasonography-magnetic resonance imaging fusion-guided prostate biopsy," *BJU international*, vol. 101, no. 7, pp. 841–845, 2008.

[61] F. L. Bookstein, *Morphometric tools for landmark data: geometry and biology.* Cambridge University Press, 1997.

[62] W. Qiu, J. Yuan, E. Ukwatta, D. Tessier, and A. Fesnter, "3D prostate segmentation using level set with shape constraint based on rotational slices for 3D end-firing trus guided biopsy," *Medical physics*, vol. 40, no. 7, pp. 072903–1, 2013.

[63] W. Qiu, J. Yuan, E. Ukwatta, Y. Sun, M. Rajchl, and A. Fenster, "Prostate seg-
    mentation: An efficient convex optimization approach with axial symmetry using
    3D TRUS and MR images," *IEEE Transactions on Medical Imaging*, 2014.

[64] G. Litjens, R. Toth, W. van de Ven, C. Hoeks, S. Kerkstra, B. van Ginneken, G. Vin-
    cent, G. Guillard, N. Birbeck, J. Zhang, *et al.*, "Evaluation of prostate segmentation
    algorithms for MRI: the promise12 challenge," *Medical Image Analysis*, vol. 18, no. 2,
    pp. 359–373, 2014.

Appendix A

Proofs of Theorems

A.1   Proof of Prop. 2.2.1

Proof In view of the conjugate representation of the convex quadratic function

$$\frac{c}{2}\,v^2 \;=\; \max_t \; t \cdot v \;-\; \frac{1}{2c}\,t^2\,, \tag{A.1}$$

we can equally rewrite the first term of (2.3) as follows

$$\frac{1}{2}\int (P + \nabla P \cdot h)^2 dx$$

$$= \; \max_{w(x)} \int w(P + \nabla P \cdot h)dx - \frac{1}{2}\int w^2 dx\,. \tag{A.2}$$

75

On the other hand, we also have

$$\frac{\alpha}{2} \sum_{i=1}^{3} \int |\nabla (u_i + h_i)|^2 \, dx$$

$$= \max_{q} \sum_{i=1}^{3} \int \operatorname{div} q_i (u_i + h_i) dx - \frac{1}{2\alpha} \sum_{i=1}^{3} \int q_i^2 dx \,. \tag{A.3}$$

Considering (A.2) and (A.3), it is easy to see that the convex minimization problem (2.3) is mathematically equivalent to the following minimax problem:

$$\min_{h} \max_{w,q} \int w(P + \nabla P \cdot h) dx + \sum_{i=1}^{3} \int \operatorname{div} q_i (u_i + h_i) dx$$

$$- \frac{1}{2} \int w^2 dx - \frac{1}{2\alpha} \sum_{i=1}^{3} \int q_i^2 dx \,, \tag{A.4}$$

i.e.

$$\min_{h} \max_{w,q} \int \left(wP + \sum_{i=1}^{3} u_i \operatorname{div} q_i \right) dx - \frac{1}{2} \int w^2 dx$$

$$- \frac{1}{2\alpha} \sum_{i=1}^{3} \int q_i^2 dx + \sum_{i=1}^{3} \int h_i (w \cdot \partial_i P + \operatorname{div} q_i) dx \,, \tag{A.5}$$

which is called the *primal-dual formulation* in this paper.

After variation by $h_i(x)$, $i = 1, 2, 3$, the minimization of the *primal-dual formulation* (A.5) gives rise to the linear equalities' constraints

$$(w \cdot \partial_i P + \operatorname{div} q_i)(x) = 0 \,, \quad i = 1, 2, 3 \,; \tag{A.6}$$

and the maximization problem

$$\max_{w,q} E(w, q) := \int (wP + \sum_{i=1}^{3} u_i \operatorname{div} q_i) dx - \frac{1}{2} \int w^2 dx$$

$$- \frac{1}{2\alpha} \sum_{i=1}^{3} \int q_i^2(x) dx \tag{A.7}$$

in combination. Therefore, Prop. 2.2.1 is proved.

Curriculum Vitae

Name:	Yue Sun
Post-Secondary Education and Degrees:	Huazhong University of Science and Technology Wuhan, P.R.China 2006 - 2010 BSc. in Biomedical Engineering
Honours and Awards:	Western Graduate Research Scholarship (WGRS) The University of Western Ontario, London, ON 2011-2014 Poster Honorable Mention Award SPIE Medical Imaging 2014 San Diego, CA
Related Work Experience:	Teaching Assistant The University of Western Ontario London, ON 2011 - 2013

Publications:

Peer Reviewed Journal Manuscripts:

Submitted:

[1] <u>Yue Sun</u>, Jing Yuan, Wu Qiu, Martin Rajchl, Cesare Romagnoli, Aaron Fenster.

Three-Dimensional Non-Rigid MR-TRUS Registration Using Dual Optimization. Sub-

mitted to IEEE Transactions on Medical Imaging, Nov 2013. Manuscript#2013-0816

Non-Peer Reviewed Journal Manuscripts:

Published:

[1] <u>Yue Sun</u>, Wu Qiu, Cesare Romagnoli, Aaron Fenster. 3D Non-Rigid Surface-Based MR-TRUS Registration for Image-Guided Prostate Biopsy. SPIE Medical Imaging, pp. 90362J-90362J, International Society for Optics and Photonics, 2014

[2] Shaobin Chen, Mingyue Ding, Chao Cai, Xiaowei Fu, <u>Yue Sun</u>, Duo Chen. Design and Implementation of Knowledge-Based Framework for Ground Objects Recognition in Remote Sensing Images. Proc. SPIE 7498, 749832, 2009

Peer-Reviewed Conference Proceedings:

Published:

[1] <u>Yue Sun</u>, Jing Yuan, Martin Rajchl, Wu Qiu, Cesare Romagnoli, Aaron Fenster. Efficient Convex Optimization Approach to 3D Non-Rigid MR-TRUS Registration. MICCAI 2013, LNCS 8149, 195-202, 09/2013

[2] Wu Qiu, Jing Yuan, Eranga Ukwatta, <u>Yue Sun</u>, Martin Rajchl, Aaron Fenster. Fast Globally Optimal Segmentation of 3D Prostate MRI with Axial Symmetry Prior. MICCAI 2013, LNCS 8150, 198-205, 09/2013

[3] Jing Yuan, Eranga Ukwatta, Wu Qiu, Martin Rajchl, <u>Yue Sun</u>, Xue-Cheng Tai, Aaron Fenster. Jointly Segmenting Prostate Zones in 3D MRIs by Globally Optimized Coupled Level-Sets. EMMCVPR 2013, LNCS 8081, 12-25, 08/2013

[4] Jing Yuan, Wu Qiu, Eranga Ukwatta, Martin Rajchl, <u>Yue Sun</u>, Aaron Fenster. An

Efficient Convex Optimization Approach to 3D Prostate MRI Segmentation with Generic Star Shape Prior. Prostate MR Image Segmentation Challenge, MICCAI 2012

National, Provincial and Local Conference Presentations:

[1] <u>Yue Sun</u>, Jing Yuan, Cesare Romagnoli, Aaron Fenster. Three-Dimensional Non-Rigid MR-TRUS Registration Using Duality-Based Optimization Method. Imaging Network Ontario Symposium (ImNO). 03/2014

[2] <u>Yue Sun</u>, Jing Yuan, Cesare Romagnoli, Aaron Fenster. Three-Dimensional MR-TRUS Registration for Image-Guided Prostate Biopsy. CIHR TEAM GRANT & OICR SMARTER IMAGING PROGRAM (SIP) - Imaging Applications in Prostate Cancer Workshop. 11/2013

[3] <u>Yue Sun</u>, Jing Yuan, Cesare Romagnoli, Aaron Fenster. MR to Ultrasound Registration for Image-Guided Prostate Biopsy. Canadian Organization of Medical Physicists (COMP). 09/2013

[4] <u>Yue Sun</u>, Jing Yuan, Cesare Romagnoli, Aaron Ward, Aaron Fenster. Magnetic Resonance to Ultrasound Registration for Image-Guided Prostate Biopsy. London Imaging Discovery (LID). 06/2013

[5] <u>Yue Sun</u>, Jing Yuan, Cesare Romagnoli, Aaron Fenster. Magnetic Resonance to Ultrasound Registration for Image-Guided Prostate Biopsy. London Health Research Day. 03/2013

[6] <u>Yue Sun</u>, Jing Yuan, Cesare Romagnoli, Aaron Fenster. Magnetic Resonance to Ultrasound Registration for Image-Guided Prostate Biopsy. Imaging Network Ontario Symposium (ImNO). 02/2013

[7] <u>Yue Sun</u>, Cesare Romagnoli, Aaron Ward, Aaron Fenster. Magnetic Resonance to Ultrasound Registration for Image-Guided Prostate Biopsy. CIHR TEAM GRANT & OICR SMARTER IMAGING PROGRAM (SIP) - Imaging Applications in Prostate Cancer Workshop. 11/2012

[8] <u>Yue Sun</u>, Cesare Romagnoli, Aaron Ward, Aaron Fenster. Magnetic Resonance to Ultrasound Registration for Image-Guided Prostate Biopsy. London Health Research Day. 03/2012

Invited Talks:

[1] Lecture Series: Robarts Research MedIA Series - Medical Image Analysis Modern Optimization Analysis, Algorithms and Clinical Applications,

London, ON. 08/2013

Presentation Title: Dual-Optimization Method to 3D Prostate MRI-TRUS Deformable Registration

[2] Lecture Series: Huazhong University of Science and Technology,

Wuhan, China. 10/2012

Presentation Title: MR to Ultrasound Registration for Image-Guided Prostate Biopsy